NAVAL POSTGRADUATE SCHOOL

MONTEREY, CALIFORNIA

THESIS

SHEAR AND STABILITY AT THE BASE OF THE MIXED LAYER IN THE ARCTIC OCEAN: THE ROLE OF INERTIAL MOTIONS

by

George Young Suh

March 2011

Thesis Advisor: Timothy Stanton
Second Reader: William Shaw

Approved for public release; distribution is unlimited

THIS PAGE INTENTIONALLY LEFT BLANK

REPORT DOCUMENTATION PAGE			Form Approved OMB No. 0704-0188
Public reporting burden for this collection of information is estimated to average 1 hour per response, including the time for reviewing instruction, searching existing data sources, gathering and maintaining the data needed, and completing and reviewing the collection of information. Send comments regarding this burden estimate or any other aspect of this collection of information, including suggestions for reducing this burden, to Washington headquarters Services, Directorate for Information Operations and Reports, 1215 Jefferson Davis Highway, Suite 1204, Arlington, VA 22202-4302, and to the Office of Management and Budget, Paperwork Reduction Project (0704-0188) Washington DC 20503.			
1. AGENCY USE ONLY ***(Leave blank)***	**2. REPORT DATE** March 2011	**3. REPORT TYPE AND DATES COVERED** Master's Thesis	
4. TITLE AND SUBTITLE Shear and Stability at the Base of the Mixed Layer in the Arctic Ocean: The Role of Inertial Motions		**5. FUNDING NUMBERS** **N/A**	
6. AUTHOR(S) George Y. Suh			
7. PERFORMING ORGANIZATION NAME(S) AND ADDRESS(ES) Naval Postgraduate School Monterey, CA 93943-5000		**8. PERFORMING ORGANIZATION REPORT NUMBER** **N/A**	
9. SPONSORING /MONITORING AGENCY NAME(S) AND ADDRESS(ES) N/A		**10. SPONSORING/MONITORING AGENCY REPORT NUMBER** **N/A**	
11. SUPPLEMENTARY NOTES The views expressed in this thesis are those of the author and do not reflect the official policy or position of the Department of Defense or the U.S. Government. IRB Protocol number _____N/A_____.			
12a. DISTRIBUTION / AVAILABILITY STATEMENT Approved for public release; distribution is unlimited		**12b. DISTRIBUTION CODE** A	

13. ABSTRACT (maximum 200 words)

The Arctic environment changed significantly over recent decades and declines in perennial sea ice and thickness concentrations have been frequently observed. Current predictive models providing researchers with conservative estimates of sea ice concentrations, the lack of observations and understanding of the physical processes that promote changes in sea ice create inaccuracies that need to be improved. A fusion of buoy observations, satellite derived ice concentrations, and modeled wind data are made in this thesis to provide a better insight into sea ice inertial motions and its influence on the processes that occur in the Arctic Ocean mixed layer and to investigate whether these processes can be parameterized to improve predictive models.

Observations made in the Canadian Basin and the Transpolar Drift by high resolution Autonomous Ocean Flux Buoys (AOFBs), SSMI and AMSR-E satellite derived ice concentrations, and ERA-Interim winds are used to examine the relationships between winds, ice coverage and sea ice inertial oscillations. Data collected from AOFBs and collocated Ice-Tethered Profilers (ITPs) are analyzed to investigate whether ocean mixed layer inertial oscillations contribute to shear instability at the base of the mixed layer, which serves as a mechanism for vertical transport of heat in water masses underlying the mixed layer.

Results show that simple linear regression models cannot explain the relationship between inertial sea ice velocities and modeled winds. However, they do indicate that the magnitude of the inertial sea ice velocities during summers is greater when compared to winter. Analysis further reveals a relationship between sea ice inertial oscillations and sea ice concentrations. We conclude that parameterizing the conditions that permit significant inertial motions in terms of changing areal ice conditions is viable. Inertial oscillations generated in the Arctic Ocean mixed layer do contribute significantly to the instability at the base of the mixed layer, especially during summers. However, comparisons of dynamic instability at the base of the mixed layer to satellite derived sea ice concentrations reveal no conclusive relationship.

14. SUBJECT TERMS Arctic Ocean, Inertial Motion, Inertial Oscillations, Shear velocity, Dynamic Stability, Sea Ice, Mixed Layer, Ice Concentration, Autonomous Ocean Flux Buoy, Ice-Tethered Profiler, SSMI, AMSR-E, ECMWF, Oceanic Forcing, Canada Basin, Beaufort Sea, Transpolar Drift.			**15. NUMBER OF PAGES** 99
			16. PRICE CODE
17. SECURITY CLASSIFICATION OF REPORT Unclassified	**18. SECURITY CLASSIFICATION OF THIS PAGE** Unclassified	**19. SECURITY CLASSIFICATION OF ABSTRACT** Unclassified	**20. LIMITATION OF ABSTRACT** UU

NSN 7540-01-280-5500 Standard Form 298 (Rev. 2-89)
Prescribed by ANSI Std. 239-18

THIS PAGE INTENTIONALLY LEFT BLANK

Approved for public release; distribution is unlimited

SHEAR AND STABILITY AT THE BASE OF THE MIXED LAYER IN THE ARCTIC OCEAN: THE ROLE OF INERTIAL MOTIONS

George Y. Suh
Lieutenant, United States Navy
B.S., University of California Los Angeles, 2001

Submitted in partial fulfillment of the
requirements for the degree of

MASTER OF SCIENCE IN METEOROLOGY AND PHYSICAL OCEANOGRAPHY

from the

NAVAL POSTGRADUATE SCHOOL
March 2011

Author: George Y. Suh

Approved by: Timothy Stanton
Thesis Advisor

William Shaw
Second Reader

Jefferey D. Paduan
Chair, Department of Oceanography

THIS PAGE INTENTIONALLY LEFT BLANK

ABSTRACT

The Arctic environment changed significantly over recent decades and declines in perennial sea ice and thickness concentrations have been frequently observed. Current predictive models providing researchers with conservative estimates of sea ice concentrations, the lack of observations and understanding of the physical processes that promote changes in sea ice create inaccuracies that need to be improved. A fusion of buoy observations, satellite derived ice concentrations, and modeled wind data are made in this thesis to provide a better insight into sea ice inertial motions and its influence on the processes that occur in the Arctic Ocean mixed layer and to investigate whether these processes can be parameterized to improve predictive models.

Observations made in the Canadian Basin and the Transpolar Drift by high resolution Autonomous Ocean Flux Buoys (AOFBs), SSMI and AMSR-E satellite derived ice concentrations, and ERA-Interim winds are used to examine the relationships between winds, ice coverage and sea ice inertial oscillations. Data collected from AOFBs and collocated Ice-Tethered Profilers (ITPs) are analyzed to investigate whether ocean mixed layer inertial oscillations contribute to shear instability at the base of the mixed layer, which serves as a mechanism for vertical transport of heat in water masses underlying the mixed layer.

Results show that simple linear regression models cannot explain the relationship between inertial sea ice velocities and modeled winds. However, they do indicate that the magnitude of the inertial sea ice velocities during summers is greater when compared to winter. Analysis further reveals a relationship between sea ice inertial oscillations and sea ice concentrations. We conclude that parameterizing the conditions that permit significant inertial motions in terms of changing areal ice conditions is viable. Inertial oscillations generated in the Arctic Ocean mixed layer do contribute significantly to the instability at the base of the mixed layer, especially during summers. However, comparisons of dynamic instability at the base of the mixed layer to satellite derived sea ice concentrations reveal no conclusive relationship.

THIS PAGE INTENTIONALLY LEFT BLANK

TABLE OF CONTENTS

LIST OF FIGURES

LIST OF TABLES

THIS PAGE INTENTIONALLY LEFT BLANK

LIST OF ACRONYMS AND ABBREVIATIONS

ADCP	Acoustic Doppler Current Profiler
AMSR-E	Advanced Microwave Scanning Radiometer – Earth Observing System
AOFB	Autonomous Ocean Flux Buoys
CO_2	Carbon Dioxide
CNO	Chief of Naval Operations
CTD	Conductivity Temperature Depth
DMSP	Defense Meteorological Satellite Program
ECMWF	European Center for Medium-Range Weather Forecasts
ERA-Inertim	European Center for Medium Forecasts Experimental Analysis Interim
GCM	Global Circulation Model
GMT	Greenwich Mean Time
GPS	Global Positioning System
$GtCO_2$	Gigatons of CO_2
IBO	Ice-Based Observatories
IPCC	Intergovernmental Panel on Climate Change
ITP	Ice-Tethered Profiler
MLD	Mixed Layer Depth
N^2	Brunt-Vaisala Frequency
NASA	National Aeronautics and Space Administration
NPS	Naval Postgraduate School
NSPD-66	National Security Presidential Directive – 66
PHC	Polar Science Hydrographic Climatology
Ri	Richardson Number

SHEBA	Surface Heat Budget of the Arctic Experiment
SLTC	Steady Local Turbulence Closure
SSMI	Special Sensor Microwave Imager
TFCC	Task Force Climate Change
UNCLOS	United Nations Convention on the Law of the Sea
WHOI	Woods Hole Oceanographic Institute
YD	Yearday

ACKNOWLEDGMENTS

I want to express my deep and sincere gratitude to my thesis advisor, Professor Tim Stanton, first for entrusting me to explore his vision and then for his continued enthusiasm, guidance, motivation and patience. Thank you for the opportunity.

I am also gratefully indebted to my co-advisor Professor Bill Shaw for his sound advice and patience. I would have been lost without your expertise and experience.

Last but not least, I want to thank my beautiful wife, Fiona, for the enduring support and strength she provided me in achieving this degree and completing this thesis. You are the world to me and I love you more every day.

THIS PAGE INTENTIONALLY LEFT BLANK

I. INTRODUCTION

A. MOTIVATION

1. Global Climate Change

Technological revolutions over the past century fuelled global agricultural and industrial growth and changed the way mankind interacts with the earth. While such advances undoubtedly improved our lives, they came at a price, as human footprints left increasingly large and irreversible marks on our environment. Our dependency on fossil fuels drives increasing atmospheric concentrations of carbon dioxide (CO_2), adding to the pre-existing greenhouse gases and aerosols in the atmosphere. During the preindustrial age, CO_2 concentrations were approximately 280 parts per million (ppm), whereas measurements taken in 2005 show a dramatic increase to 379 ppm. Emissions of CO_2 from fossil fuels remained at an annual average of 6.4 Gigatons of CO_2 ($GtCO_2$) during the 1990's and increased to 7.2 $GtCO_2$ during the period between 2000–2005. Overwhelming evidence exists proving that these anthropogenic sources, in conjunction with aerosols, not only increased the average global temperature, but caused other noticeable changes in the earth's climate (Intergovernmental Panel on Climate Change Fourth Assessment Report (IPCC AR4), 2007).

2. Arctic Change

Observed increases in global temperatures resulted in Arctic amplification that manifested in an increased melting of sea ice (IPCC AR4, 2007). Over the past several decades, the September sea ice extent has decreased at alarming rates (Stroeve et al., 2007). As seasonal sea ice continues to decline, access to the Arctic by commercial and civilian vessels will inevitably increase due to the shorter distances these vessels will need to travel from both the Pacific and Atlantic Oceans. In addition, the accessibility and availability of natural resources along the continental shelves in the Arctic will increase, thereby rousing the economic interests of nations that border the Arctic region (i.e., United States, Russia, Canada, Greenland, Iceland, Denmark, and Norway) (NSPD-

66, 2009). Subsequently, territorial disputes that have yet to be considered by the United Nations Convention on the Law of the Sea (UNCLOS) already have, and will continue to manifest. An example of such a dispute concerns the Northwest Passage, which many nations consider an international strait. However, the Canadian government claims it as internal waters. Historically, political tensions between nations have always involved their respective military forces, and it is fair to assume that the Arctic region will require a military presence in the near future. Responding to the potential need, the United States tasked the U.S. Navy to create the Task Force Climate Change (TFCC), a Task Force responsible for advising the Chief of Naval Operations (CNO) on Arctic and climate related affairs (TFCC, 2009). It is politically and militarily imperative that future Arctic conditions are forecasted with increased accuracy in order to allow for proper planning and policy making.

3. Arctic Sea Ice Decline

For many years, models predicted that the Arctic region would be most sensitive to climate change compared to any other region in the world (Zhang and Walsh, 2006). Recent measurements and observations made by Zhang and Walsh (2006) confirm these predictions. As part of an international effort, the Intergovernmental Panel on Climate Change (IPCC), Zhang and Walsh (2006) assessed a comprehensive number of coupled ocean-atmospheric numerical models that demonstrated current and future climate scenarios. Assessments were made based on two types of simulations - one considering twentieth century greenhouse gas emissions and the other that of the twenty-first century. The Panel then used an ensemble mean approach to determine a credible estimate of changes in sea ice produced. The models were able to illustrate decreases in ice area during the last thirty years of the twentieth century (1979–1999) to within 20% of the observed climatology. More recently, in the last decade, the same measures illustrated a similar decline in sea ice area demonstrating that these models have the ability to reliably portray the environment's climate. However, it is important to note that observed sea ice extent declines are occurring at a more rapid pace than modeled predictions. Empirical observations collected in the time period between 1953–2006 have shown an accelerating

trend of Arctic sea ice extent decline below the IPCC assessed modeled September average sea ice extent (Stroeve et al., 2007). Comparing the observed Arctic sea ice extent to 13 IPCC AR4 models, Figure 1, Stroeve et al. (2007) observed that between 1953–2006 there was a -7.8 ± 0.6 %/decade decrease in sea ice extent, which is three times larger than the multi-model mean trend of -2.5 ± 0.2%/decade. This suggests that these models as a group do not forecast September sea ice extent in an accurate manner and that the Arctic might become an ice free ocean sooner than predicted.

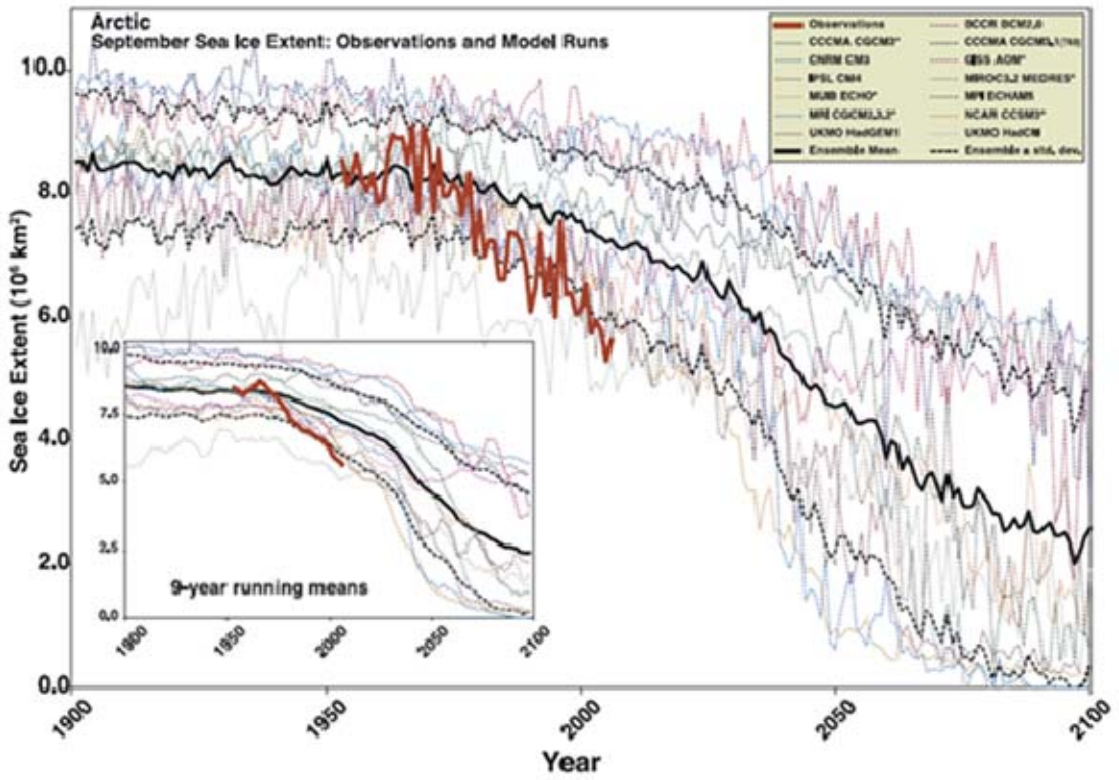

Figure 1. Arctic September sea ice extent (x 10^6 km^2) from observations (thick red line) and 13 IPCC AR4 climate models, together with the multi-model ensemble mean (solid black line) and standard deviation (dotted black line). Models with more than one ensemble member are indicated with an asterisk. Inset shows 9-year running means. (From Stroeve et al., 2007)

Two main processes contribute to Arctic sea ice extent/ice volume decline: near-surface warming from ocean-ice-albedo feedback and ocean advection of heat below the

Arctic Ocean mixed layer. Both Ice-Albedo Feedback and advection of warmer waters from the Pacific and the Atlantic Oceans, contribute to increased ice melt and freshening of the mixed layer.

The Ice-Albedo Feedback is a positive feedback loop, a continuing cycle that acts to increase the outcome of its previous result. Albedo is a surface's ability to reflect light or, in this case, solar radiation. A surface that is entirely reflective has an albedo of 100% or 1, and a surface with zero reflectivity or a black body has an albedo of 0 (zero). Albedo varies with seasons and within regions due to the widely differing of snow covered ice (with albedos of 0.8–0.9) and open ocean and melting ice (with albedos of 0.1 in leads, 0.2 in dark ponds, 0.4 in light ponds, and 0.6–0.7 in melting multiyear ice) (Perovich, 2002).

Albedo changes are critical to the Arctic surface energy budget and regulates heat budgets in the atmosphere, sea ice cover, and upper ocean. In the Arctic, the largest absorber of solar radiation is the ocean, since its characteristics are similar to that of a black body. As ice extent decreases from climate change, the ocean continues to become more exposed to solar radiation. This radiation is absorbed by the ocean, yielding a further increase in ocean and atmospheric temperatures. Increased ocean and atmospheric temperatures causes additional melting of ice. The additional melting exposes more of the ocean's surface to solar radiation and the temperatures of the ocean and atmosphere continues to rise in a persistent cycle known as a positive feedback loop. This positive feedback loop also works in reverse. If the net albedo of the Arctic Ocean were to increase through increased summer-time ice cover, more solar radiation would be reflected off the earth's surfaces causing ocean and atmospheric temperatures to cool. As a result, ice will grow in a cyclical loop, building upon former results. Thus, the effects of the Ice-Albedo Feedback, specifically the positive feedback loop, on the mixed layer heat can stimulate sea ice melt.

Sea ice ablation (melting of ice) can also result from advection of Pacific Ocean water via the Bering Strait, or Atlantic Ocean water through the Fram Strait or Nordic Seas. The Pacific and Atlantic Ocean waters are warm compared to polar mixed layer

water but saltier and therefore denser, which makes it less buoyant. As a result these warm water layers are emplaced below the Arctic Ocean mixed layer, and vertical transport processes are required to make that heat available for melting the bottom of sea ice. This phenomenon was one of many studies conducted during the Surface Heat Budget of the Arctic Experiment (SHEBA), which was conducted to better understand the Arctic atmosphere/sea ice/ocean system. Specifically, research done by Shaw et al., (2009) and Perovich et al. (2003) determines that the thickness of sea ice can be significantly altered by bottom melting. Both studies analyzed data collected during SHEBA, a yearlong (from 1997-1998) interdisciplinary expedition on an ice drift camp deployed in the middle of the Beaufort Gyre and terminating in the western Arctic.

Perovich et al. (2003) monitored ice accretion and ablation at 135 sites. During the experiment, weather conditions at site locations in 1998 experienced a slightly colder than average winter (cooler by 0.6°C), and a longer than normal melt season (80 days versus an average of 55 days). To account for the spatial variability in the sea ice cover, ice mass balances were taken on first-year ice, ponded ice, unponded ice, multiyear ice, hummocks, new ridges, and old ridges. Analysis of the combined results from all the sites found an average sea ice winter growth of 0.51 m and a summer melt of 1.26 m. The melt consisted of 0.64 m of surface melt and 0.62 m of bottom melt. The bottom melt measured during this experiment is noted to be more than twice the amount reported from any previous experiments, with its peak coinciding with an incident of a sharp increase in ice drift and divergence. It was also noted that local solar radiation inputs were not sufficient to account for the measured bottom ablation, which peaked in early August and also coincided with a sharp increase in ice drift and divergence. These results demonstrate that bottom melting of sea ice is comparable to surface melting.

A noticeable change in sea ice due to bottom melt was also observed by Shaw et al. (2009). Using the SHEBA observations of the T/S structure and thermal dissipation rate estimates of vertical heat fluxes from the pycnoline in conjunction with data from the Steady Local Turbulence Closure (SLTC) model, a numerical ice ocean boundary layer model, the researchers investigated the contribution of the upper ocean to the ice cover

energy balance over the year-long observation period. The ice cover energy budget was most affected by entrainment heat fluxes during the middle period of the record where the SHEBA site drifted over the Northwind Ridge and the Chukchi Shelf. The study observed a significant increase in upper pycnocline heat content and a reduction in upper pycnocline stratification due to the presence of relatively warm and salty Pacific origin water, which allowed for moderate pycnocline heat fluxes (here heat flux is the vertical turbulent transfer rate of heat) (2.1–3.7 W m^{-2}) and moderate ocean-to-ice heat fluxes (3.5 W m^{-2}). During this portion of the drift, the ocean's contribution to the ice cover energy budget caused a 15% reduction in winter ice growth due to the entrainment of heat stored in the upper pycnocline. During summer, the ocean to ice heat flux estimates were larger than the latent energy changes associated with basal melting. Evidence thus indicates that heat fluxes across the base of the surface mixed layer affects sea ice, but the dominant source of bottom melting was still summer insolation.

4. Modeling of the Arctic

As suggested by Shaw et al. (2009), it is difficult to model all the small-scale Arctic mixed layer processes within coupled ocean-ice-atmosphere models that are used to predict future climate changes. In general, global modeling is challenging, because it is difficult to simulate the nonlinearities and fine spatial and/or time scales involved in the small-scale processes that occur in the real environment. Arbetter et al. (1997) shows that Arctic sea ice models have different responses to atmospheric and oceanic heat flux perturbations. As a result, global circulation model (GCM) predictions are dependent on the choice of sea ice models. Curry et al. (1995) performed a study resulting in a similar conclusion where a number of one-dimensional sea ice models with comparable annually averaged sea ice thickness for present day forcing showed a substantial difference to sensitivity to surface heat flux perturbations and ice-albedo feedback. The inaccuracies of sea ice models also result from many models' inabilities to resolve resolutions finer than the Rossby radius of deformation (a length scale at which the earth's rotational effects become just as important as buoyancy or gravity wave effects in the evolution of a flow about a disturbance). In the Arctic, the Rossby radius of deformation is typically to

be 5–10 km. The current inability of models to resolve to such small scales makes it difficult to simulate small scale processes and lateral transport by ocean eddies.

Unfortunately, because the Arctic is such a remote and harsh environment, observations and in-situ measurements are difficult to obtain. The majority of existing information was gathered in the past via satellite remote sensing. Accordingly, historical observations and validations regarding the region are sparse, making the task of modeling the Arctic environment a very difficult endeavor. This lack of understanding of the physical processes that govern the Arctic climate is also compounded by the limitations in computer processing and model physics. An important priority in attempting to model this sparsely sampled environment is to understand the physical processes that occur in the coupled atmosphere-ice-ocean system, including processes that occur at the base of the ocean surface mixed layer. This thesis will investigate whether oceanic inertial motions, a sub grid scale effect in GCMs, contribute to the entrainment of heat from the deeper warmer ocean, stimulating the reduction in sea ice extent in different regions and seasons. The relationship between inertial motion magnitude and changing areal ice concentrations are investigated to determine if these conditions can be parameterized and incorporate these factors into predictive models. In order to do so, relationships between wind forcing, ice concentration, and sea ice motion are analyzed.

B. ARCTIC SURFACE MIXED LAYER: DESCRIPTION AND DYNAMICS

1. Arctic Mixed Layer

The bulk of the research for this thesis focuses on mixed layer dynamics and stability as well as the entrainment across the base of the mixed layer (Shaw et al., 2009 and Yang et al., 2004). The surface mixed layer is the part of the water column extending down from the ice/ocean interface characterized by nearly uniform temperatures and densities that reach from tens to hundreds of meters below the surface of the ocean. It is created by the mixing of water properties as a result of surface wind stress or its resulting waves, or by convective processes, typically driven by brine rejection during ice formation. In the ice-covered Arctic, the mixed layer is at or very near the freezing point

as departures from this temperature rapidly result in ice formation or ice melt. The depth of the mixed layer is delineated by a very sharp and localized density gradient, which is determined by the applied surface forcing (wind stress or buoyancy) and the strength of the underlying stratification. The ratio of these two competing factors defines the gradient Richardson number, which will be described in more detail in the following sections.

Stratification at the base of the mixed layer in the Arctic Ocean varies seasonally, summer heating results in an increase in freshwater introduction from either river runoffs or directly from sea ice melt. This addition of freshwater locally strengthens the stratification, thereby decreasing the tendency for entrainment from the pycnocline. During winters, sea ice is formed from relatively freshwater leaving behind a comparably denser saline stratified water column, which reduces the stratification at the base of the mixed layer. The stratification that develops during different seasons serves as a barrier to mixing between the surface mixed layer and the deeper and warmer ocean waters beneath.

In addition to seasonal variability, the strength of the stratification in the mixed layer is also varies regionally based on proximity to river runoff and inflows from the Atlantic and Pacific Ocean. This thesis will investigate data from buoys deployed from ice floes in the Canadian Basin and along the Transpolar Drift. Regionally in the Arctic, sources of freshwater are mainly derived from major rivers, sea ice melt, and the Pacific and Atlantic Oceans. Most of the freshwater is stored in the Beaufort Gyre (Serreze et al. 2006, Figure 2). According to Serreze et al. (2006), in the Arctic Ocean, 38% of the annual freshwater input is primarily dominated by river runoffs. Freshwater content can also come from less salty warmer Pacific waters via the Bering Strait, about 30% of the total. Another source of freshwater is precipitation and this contributes about 28%. These large inputs of freshwater can produce a strong stratification barrier isolating the sea ice and surface waters from deeper and warmer ocean waters below. In the Canadian Basin, Toole et al. (2010) found that the July-August mixed layer depth averaged 16 m and the winter mixed layer depth averaged 24 m. Near the Transpolar Drift, regions of

varying freshwater content are separated by fronts, specifically, over the Nansen-Gakkel Ridge, Lomonosov Ridge, and the western Eurasian Basin between waters derived from the Canadian and Eurasian Basins (Rudels, 1996), where the Canadian and Eurasian Basin waters are influenced by the Pacific and Atlantic Oceans, respectively.

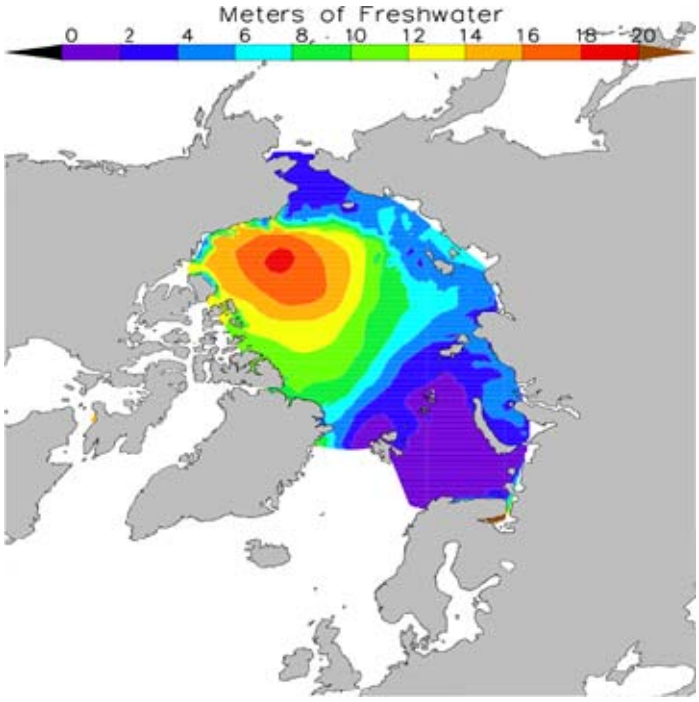

Figure 2. Mean annual freshwater content of the Arctic Ocean (excluding sea ice) based on the University of Washington Polar Science Hydrographic Climatology (PHC). The scale is in meters of freshwater, computed using a reference salinity of 34.8 (http://psc.apl.washington.edu/Climatology.html). (From Serreze et al., 2006)

The winds that flow above the surface of the ocean applies stress onto to the ocean that forces the surface of the ocean to accelerate. This in turn forces the acceleration of the ocean mixed layer. As the winds dissipate, the surface of the ocean and the mixed layer retains its momentum described as inertial motion, a process that will be described in the next section. Halpern (1974) shows that away from oceanic boundary layers and in the absence of a strong current, the depth of the mixed layer is modulated by wind forcing. Seasonal storms and fronts that pass through the Arctic generate wind stress on the surface of the open ocean, in leads, or the sea ice's surface, and disturbs the

stratification of the mixed layer by velocity shear. Velocity shear is manifested as wind driven currents are generated across the depth of the mixed layer, with the shear increasing sharply at the stratification jump at the base of the mixed layer. Consequently, in the Arctic Ocean having sufficient amounts of shear in the presence of weak stratification produces mixing and disturbs the stratification of the mixed layer, which then deepens the mixed layer (Yang, et al., 2004). These dynamic processes that occur within the mixed layer can influence the salinity and temperature of the mixed layer by entrainment, potentially affecting the thermodynamic balance of sea ice.

2. Inertial Motion

Inertia is a fundamental property of mass that describes the resistance an object possesses to changes in its state of motion or rest. In other words, unless influenced by an external force, an object at rest will remain at rest while an object in motion will remain in motion. Inertial motion of water then, describes the movement of water uninfluenced by factors of motion save for the effect of the Earth's rotation. If a current were to be set in motion and left on its own, the Coriolis force would deflect the water to the right in the Arctic (i.e., in the Northern Hemisphere), and thereby cause the water to move in a circle. If the water continued to move in a circle, this motion is characterized to be oscillating or inertial oscillation.

In the ocean mixed layer "slab", inertial motions are excited by fluctuations in winds, and decay by friction at the ice ocean interface and base of the mixed layer, and by leakage out into the pycnocline as inertial waves. This was illustrated by Pollard and Millard (1970), using a simple two layer slab mixed layer model, which showed that the generation of inertial motions in the upper ocean were a response to an initial impulse or force caused by fluctuations in the wind field under time scales less than an inertial period. (The inertial period at high latitudes (near 90°) is $T_{inert} = (T_{sidereal\ day})/(2\sin\varphi) = \sim 11.97$) They also demonstrated that the angle between the wind vector and the current vector is an important factor in determining whether momentum will be added to or removed from inertial motions. A further study by Pollard (1980), which used wind observations to initialize the model used by Pollard and Millard (1970), compared

observed inertial oscillations to the modeled inertial oscillations and determined that the forcing of inertial motions is most efficient in depressions along frontal boundaries due to the strong winds and wind shifts along the front.

Inertial motions in the ocean have specific features. A previous study by Webster (1968) suggests that inertial period motions are transient and can be found at all depths and areas of the ocean, each measure of transient motion lasting up to a week. Subsequent studies by Pollard (1970) determined that these motions constituted up to half the total kinetic energy in the ocean surfaced mixed layer. The amount of energy present was determined to be dependent on the depth of the mixed layer and less affected by the stratification or the horizontal scale of the wind stress. He also found that the large vertical velocity amplitudes observed in the mixed layer can be explained by the momentum transferred from the wind and that these velocities are confined to the top 100 m of the ocean (a depth range that spans the surface mixed layer and the upper portion of the ocean pycnocline) with the energy decreasing very rapidly with depth below the mixed layer. These facts indicate that the majority of the energy imparted into the ocean by winds can be found within the mixed layer.

A separate study by Hunkins (1967) found that sea ice motion in the Arctic is susceptible to the influences of changes in wind speed, which leads to the generation of inertial motions. According to Yang, et al. (2004), intense storms in the Beaufort Sea and Fram Strait in the Arctic can cause mechanical mixing at the base of the mixed layer. Arctic regions experience frequent storms during both the long and cold winters and the shorter and warmer summer seasons. This region is also where polar lows, small scale cyclones and/or depressions that form over open seas such as the Nordic and Bering Seas manifest and decay. These storms possess strong winds and can develop within a day, reach maximum strength in 12–24 hours, and last for several days. Polar lows then provide sufficient energy and time period required to generate inertial motions in the sea ice and ocean mixed layer. This slab like motion generates velocity shear at the base of the mixed layer.

Dissipation of inertial energy can be accomplished in two ways: via radiation of near inertial internal gravity waves (Pollard and Millard, 1970 and Pollard, 1980), or via generation of turbulence both in the mixed layer and at the base of the mixed layer. Turbulence at the base of the mixed layer leads to entrainment, which is the focus of this study.

3. Dynamic Stability and Inertial Shear

This thesis will employ the gradient Richardson number (Ri) to investigate the role of inertial shear on instability at the base of the mixed layer using observations taken from Autonomous Ocean Flux Buoys (AOFB described in the next section). The gradient Richardson number is defined as:

$$Ri = \frac{N^2}{\left(\partial \vec{u} / \partial z\right)^2}$$

This dimensionless parameter was first defined by Lewis Fry Richardson and represents the ratio between the stabilizing density gradient and destabilizing velocity. Here u represents the horizontal components of velocity and z is depth. N^2 represents the Brunt-Vaisala frequency, and defined by the following equation:

$$N^2 = \left(\frac{g}{\rho}\right)\left(\frac{d\rho}{dz}\right)$$

Here, g represents gravity and ρ represents the potential density of a parcel of fluid at a specific pressure. N^2 characterizes the frequency a parcel will oscillate at in a statically stable setting.

The dynamic stability (Ri) of a water column system is influenced by the amplitude of the local velocity shear. The system is considered to be unstable by shear enhanced mixing when Ri is below the critical value of ¼, a point at which the destabilizing shear overwhelms the stabilizing stratification. Conversely, if the

Richardson number is large, Ri > 0, the system is considered to be dynamically stable, where stratification of the system is considered to be strong and the velocity shear weak.

C. STUDY OBJECTIVES

Studies have shown that bottom melting of Arctic sea ice is comparable to surface melting. The oceanic mechanisms driving bottom melt are not fully understood. One potential mechanism is entrainment at the base of the mixed layer generated by inertial motions forced by storm driven winds. The incorporation of the effects of inertial oscillations into Arctic models and GCMs could result in improved model accuracies, as they may play an important role in influencing Arctic sea ice concentration.

The objectives of this study are to (1) investigate the relationships between wind forcing, state of the sea ice cover, and oceanic inertial oscillations and (2) investigate whether sea ice generated inertial velocities contribute to instability at the base of the mixed layer. This thesis will take into consideration the dynamic stability, stratification, region, and seasonality that maintain the composition of the mixed layer. Data collected from Autonomous Ocean Flux Buoys (AOFBs), collocated Ice-Tethered Profiles (ITPs), SSMI and AMSR-E satellite derived sea ice concentration estimates, and modeled winds from the European Center for Medium Range Forecast (ECMWF) in the Canadian Basin and Transpolar Drift will be used to examine sea ice generated inertial shear and the characteristics of the mixed layer.

THIS PAGE INTENTIONALLY LEFT BLANK

II. DATA SOURCES AND DATA PROCESSING

A. DATA SOURCES

Conducting in-situ observations of the Arctic Ocean's environment has always been a challenge due to the inaccessibility of the region, limiting our understanding of the complex physics of the ocean/ice/atmosphere system. During the past decade, the International Polar Year research and the continuing Arctic Observation Network have led to great advances in autonomous, long-term, and in-situ observations in the Arctic. In one component of these projects, the Naval Postgraduate School (NPS) and Woods Hole Oceanographic Institute (WHOI) have collocated buoys on Arctic Ocean sea ice floes (installations referred to as ice-based observatories (IBO)), allowing high resolution measurements of ocean processes and characteristics. These observations, along with publicly available data from the European Center for Medium-Range Weather Forecasts (ECMWF), the Special Sensor Microwave/Imager (SSMI), and the Advanced Microwave Scanning Radiometer—Earth Observing System (AMSR-E) will be used for this study. Data sets from these ancillary/secondary sources were available for each IBO drift.

1. Arctic Ocean Flux Buoys

Associate Research Professor Tim Stanton and his research group at NPS have developed an unattended secure platform capable of measuring properties of the ocean surface mixed layer including current profiles and vertical fluxes of heat, salt and momentum. Since 2002, the team has placed 18 Autonomous Ocean Flux Buoys (AOFB) on ice floes throughout the Arctic Ocean.

These buoys, designed and built at NPS, were developed to measure turbulent fluxes of momentum, heat, and salt in the upper ocean 5m below the sea ice. The AOFBs are comprised of several components: a buoy furnished with electronic components located at the surface containing batteries, a global positioning system (GPS), and an Iridium communication system. This surface buoy supports an instrument package suspended in the mixed layer, which is equipped with an Acoustic Doppler Current

Profiler (ADCP), and a custom designed flux package. Observations made by the system are sent to NPS twice daily by a satellite data link (NPS AOFB program website: http://www.oc.nps.edu/~stanton/fluxbuoy/index.html, 2011). Figure 3 shows a schematic overview of the AOFB.

For the purpose of this study, we will specifically utilize sea ice velocities using GPS position data that were recorded every 15 minutes, as well as ADCP velocities, which we use to derive vertical shear in the upper ocean, that were recorded every 4 hours, and at a higher resolution of every 2 hours during wind events. ADCP velocity profiles were measured at depths of every 2 m spanning from 9 m to 87 m. Data from buoys 13 and 17, both of which were deployed in the Canadian Basin, and buoys 11, 14, 15, and 20 that were deployed in the Transpolar Drift will be considered (Figure 4). It should be noted that for AOFB 11, velocities measured by the ADCP at depths of 30 m and greater were removed due to low acoustic backscatter conditions leading to high noise velocity estimates. Similarly for AOFB 13 and 20, velocities measured at depths of 52 m and greater were also removed due to low backscatter conditions. Since ADCP data sets are collected at different times, it must be interpolated onto a uniform time vector of 2 hour increments using the AOFB's initial start time and date. This is accomplished using a 1-Dimensional interpolation done by using MATLAB's interpolation function, 'interp1'. Using sharp timeseries low pass filters, the inertial and subinertial ADCP velocities are isolated from the AOFB data set in order to obtain values of inertial and subinertial shear velocities, a process that will be explored in greater detail in later sections.

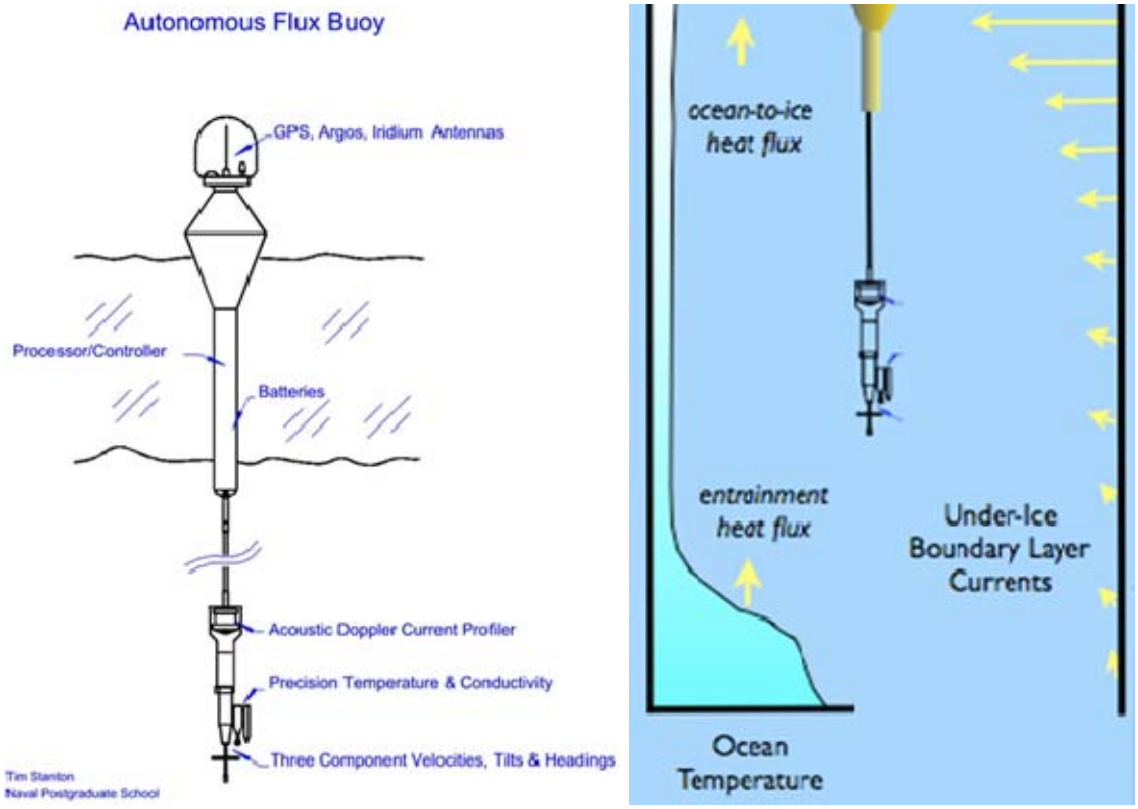

Figure 3. Overview of Naval Postgraduate School's Autonomous Ocean Flux Buoy. (From NPS AOFB program website: http://www.oc.nps.edu/~stanton/fluxbuoy/index.html, 2011)

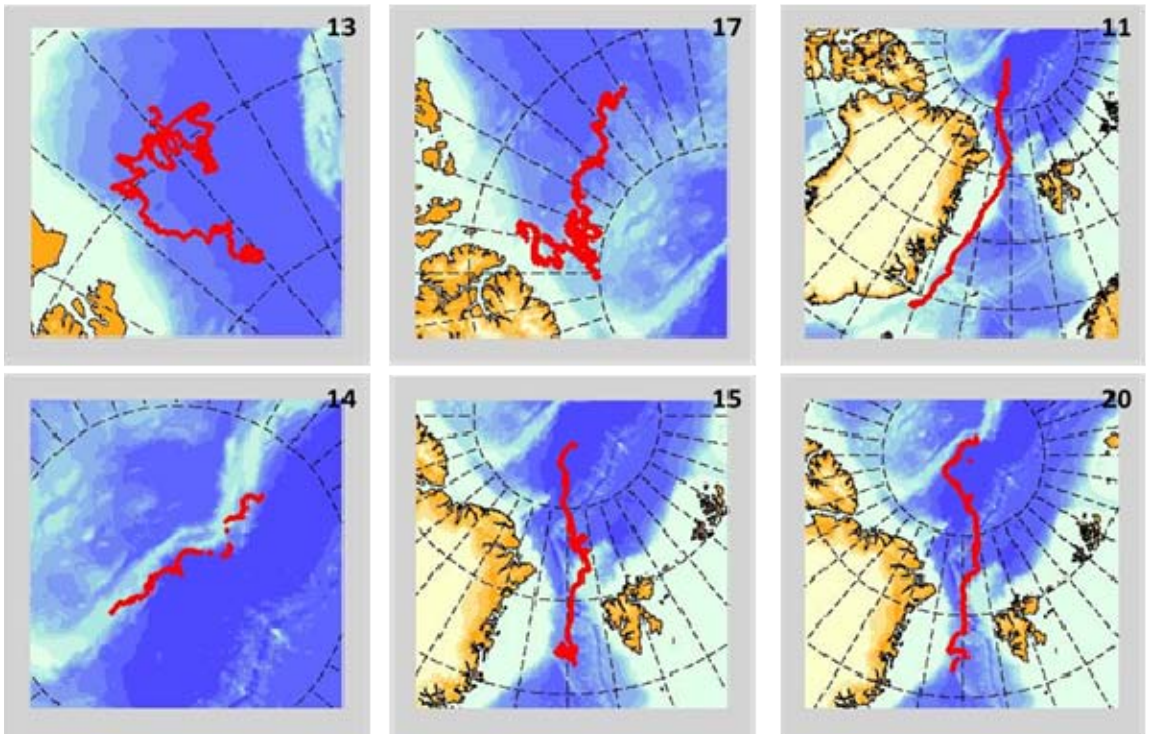

Figure 4. Drift tracks of Naval Postgraduate School's Autonomous Ocean Flux Buoy for buoys 13 and 17 located in the Canadian Basin; and, buoys 11, 14, 15, and 20 located in the Transpolar Drift. Buoy numbers are located on the upper, right hand corner of each panel. (From NPS AOFB program website: http://www.oc.nps.edu/~stanton/fluxbuoy/index.html, 2011)

2. Ice-Tethered Profilers

Collocated on the same ice floes as the AOFBs are Woods Hole Oceanographic Institute (WHOI) Ice-Tethered Profilers (ITP), which employ a Conductivity Temperature Depth (CTD) sensor developed by Sea Bird Electronics, Inc. This CTD sensor traverses along the tether of the buoy via a small traction drive wheel. The system acquires profile data based on user programmable sampling depths and schedules. Each ITP has a life span of approximately 3 years and produces an archive of recorded temperatures and pressures at 1 m vertical resolution every six hours. Depths of up to 500 to 800 m can be reached. Salinity is derived from the 1m averaged pressure, temperature, and conductivity information. Recorded data is transmitted daily to WHOI for further processing and dissemination via the Internet. For this study, real-time data

sets are downloaded. No secondary sensor response correction, calibrations or editing is applied before the data is made publicly available (WHOI program website, 2011). Figure 5 depicts an overview of the WHOI's ITP.

ITPs are collocated on the same floes as the AOFBs. These are as follows: 18 and 23 located in the Canadian Basin, and 7, 12, 19, and 38 located along the Transpolar Drift. We use the ITP data set to determine our mixed layer depth (MLD) and values of N^2. Prior to using the ITP data, each original ITP profile is screened for missing data below 15 m to allow for an accurate calculation of the mixed layer depth. ITP profiles with missing data are excluded from our analysis since they incorrectly assume a deeper mixed layer than what exists. Once the MLD and values of N^2 are determined, these values are also interpolated into 2 hour increments and time matched to the AOFB data sets using the AOFB's initial start time and date.

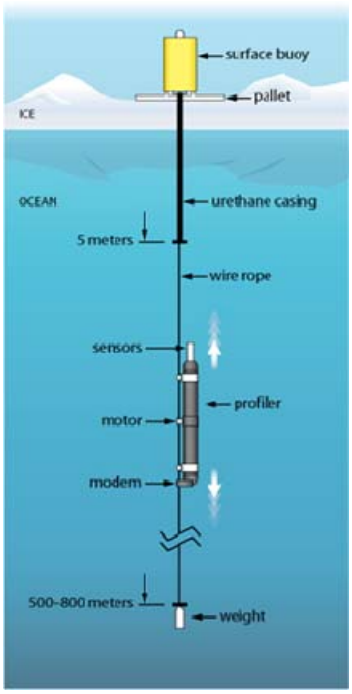

Figure 5. Overview of Woods Hole Oceaographic Institute Ice-Tethered Profiler. (From WHOI program website: http://www.whoi.edu/page.do?pid=20756, 2010)

3. Ice-Based Observatories Drift Tracks

For the remainder of this thesis, collocated AOFBs and ITPs will be called IBOs 11-7, 13-18, 14-12, 15-19, 17-23, and 20-38. IBOs 13-18 and 17-23 were located in different regions of the Canadian Basin as illustrated in Figure 6. IBOs 13-18 and 17-23 provide the largest data set for this study with a total of 1124 yeardays (YD) spanning from 2007–2010. IBO 13-18 spent most of its lifetime cycle influenced by the Beaufort Gyre and was located in the western part of the Canadian Basin. It chronicled 422 days of observations from 2007-2008. On the other hand, IBO 17-23, located in the eastern part of the Canadian Basin, drifted southward towards the Canadian Archipelagos along the western part of the Alpha Ridge and obtained 702 days of observation from 2008-2010. During Jan 2009–2010, IBO 17-23 encountered a multiyear ice pack found against the Canadian Archipelagos that kept the buoys wedged close to the continent for the remaining duration of their lifecycles. It should be noted during analysis that these conditions may potentially skew the data as the dense ice pack will act to dampen the effects of inertial motions that we seek to study in this thesis.

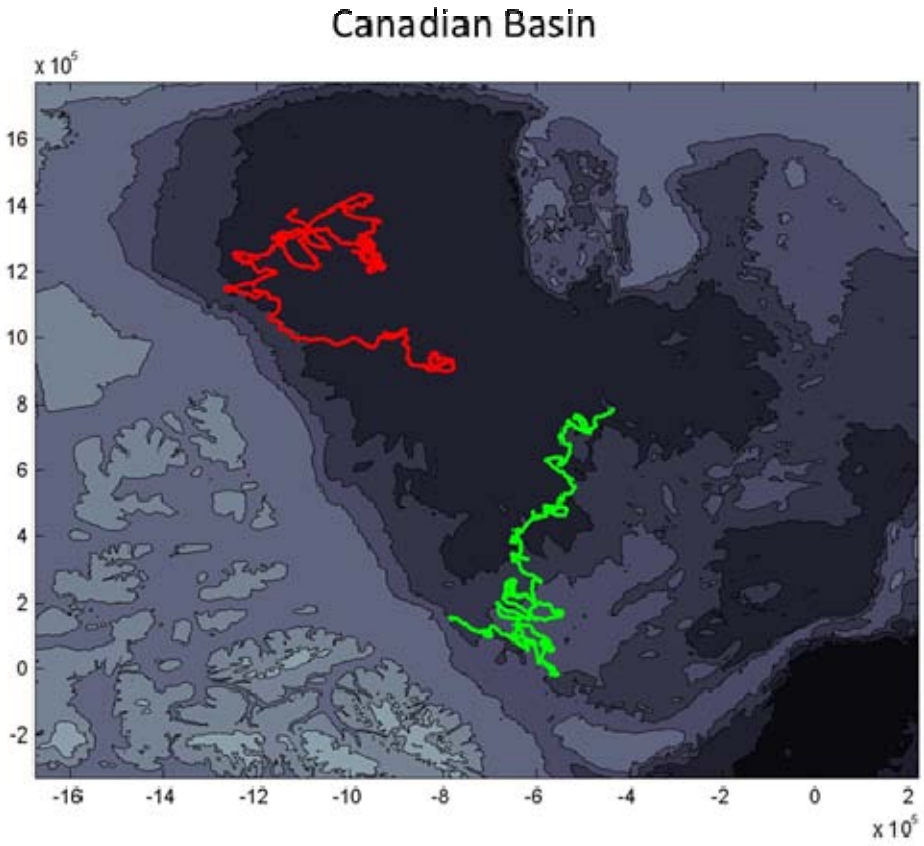

Figure 6. Bathymetric map of the Canadian Basin with drift tracks of IBOs. IBO 13-18 marked in red and IBO 17-23 marked in green.

Near the Transpolar Drift, in-situ measurements made from IBOs 11-7, 14-12, 15-19, and 20-38 are used to conduct analysis for this thesis. IBO 14-12 are the only buoys that are located at a considerable distance from the other buoys (Figure 7). IBO 14-12 drifted along the Lomonosov Ridge in the western part of the Eurasian Basin and chronicled 105 days of observations in 2007. IBO 11-7 had the longest drift track in this region and floated along the eastern continental shelf of Greenland. IBO 11-7 chronicled 181 days of observations in 2007. Both IBOs 15-19 and 20-38 chronicled 198 days of observations in 2008, and 175 days of observations in 2010. Both also had short drift tracks between Greenland and Svalbard. In total, these four IBOs provide a sum of 489 days' worth of data spanning from 2007–2008 and 2010.

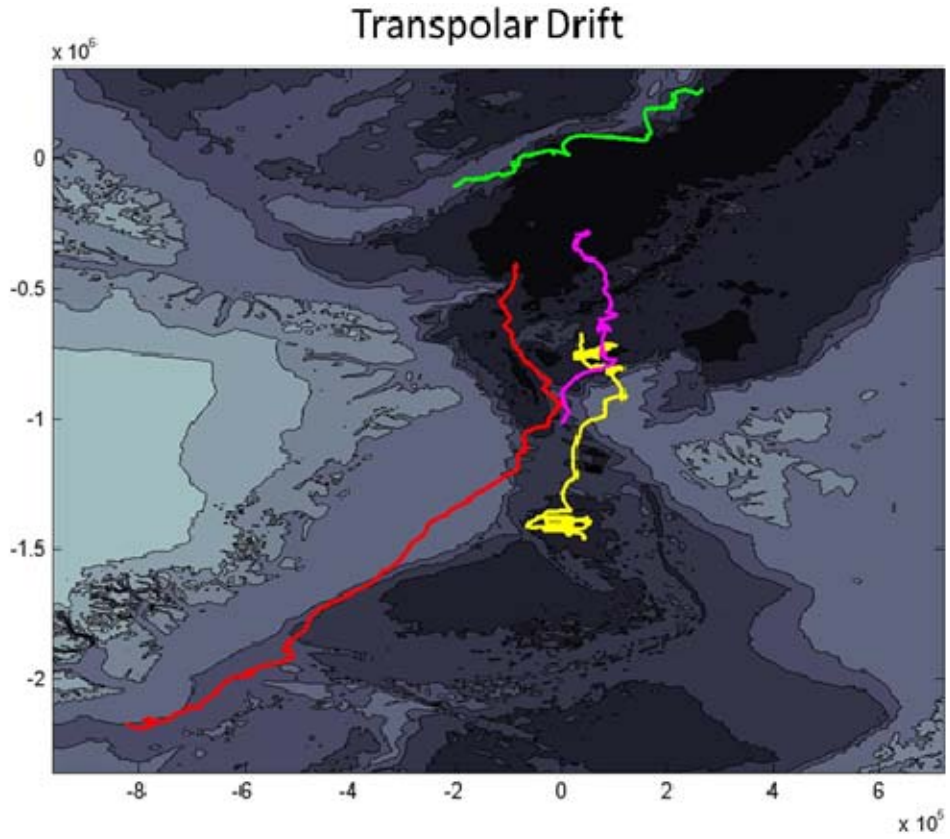

Figure 7. Bathymetric map along the Transpolar Drift with drift tracks of IBOs. IBO 11-7 marked in red, 14-12 marked in green, 15-19 marked in yellow, and 20-38 marked in magenta.

4. European Center for Medium-Range Weather Forecasts Experimental Reanalysis Interim

In-situ wind observations of the Arctic are just as sparse as oceanic observations. Further, the observations that do exist are too distant from the focus area of this research. However, the European Center for Medium-Range Weather Forecasts (ECMWF) develops a publicly accessible global circulation model re-analysis, which was used for this study. Specifically, the European Center for Medium Forecasts Experimental Analysis Interim, also known as the ERA-Inertim, is ECMWF's most recent product developed using their latest data assimilation techniques. Their archived data set spans a timeframe that covers the period between 1989 to the present day. This research uses

daily fields of 10 meter u and v wind components that are available at 1.5° x 1.5° degree resolution. The available resolution is somewhat coarse for this analysis, but is the only available source that covers the regions and times need for this research. We also use ECMWF winds for this study since these winds are commonly used in GCMs and ice models. These specific daily field parameters are found for each AOFB drift track and were available at 00, 06, 12, and 18 Greenwich Mean Time (GMT) analysis times with forecast times only available at 03 and 15. Since AOFB data sets are interpolated into 2 hour increments, the same must be done for the ECMWF data sets in order to assess comparable data points. The ECMWF data points are then time matched to the AOFB's initial start time and date.

5. Sea Ice Measurements

12.5 km resolution sea ice measurements used in this thesis were available from two different NASA programs—the Polar Pathfinder Program and the Aqua Satellite Project. The obtained sea ice measurements are also found for each AOFB drift track and time matched to our AOFB data sets using the AOFB's initial start time and date. For each AOFB data points, there are four different estimates of ice concentrations that are made with averaging circles of 15 km, 28 km, 53 km, and 100 km around each buoy location.

a. Special Sensor Microwave/Imager

As part of NASA's Polar Pathfinder Program, the Defense Meteorological Satellite Program (DMSP) outfits the Special Sensor Microwave/Imager (SSMI) on satellites F8, F10, F11, and F13. The SSMI sensor measures microwave brightness temperature of terrains, oceans, and the atmosphere. It utilizes a seven-channel, four-frequency, orthogonally polarized, passive microwave radiometric system. Frequencies at 19.35, 22.2, 37.0, and 85.5 GHz are used to collect 25 km resolution measurements and 85 GHz is used to collect 12.5 km resolution measurements. Sea ice concentration information is provided daily at the National Snow and Ice Data Center website.

b. Advanced Microwave Scanning Radiometer – Earth Observing System

The Advanced Microwave Scanning Radiometer—Earth Observing System (AMSR-E) is one of six instruments onboard NASA's Aqua satellite. The AMSR-E conducts measurements of land, ocean, and atmospheric variables utilizing a twelve channel, six frequency, conically scanning, passive microwave radiometer. It produces a Level 3 grid product (AE_SI12) of sea ice concentration and snow depth over ice that includes brightness temps at 18.7 to 89.0 GHz. The measurements are made at a 12.5 km spatial resolution. Sea ice concentration and brightness temperatures can also be found at the National Snow and Ice Data Center's website.

B. DATA PROCESSING AND ANALYSIS

1. Data Processing Method

The analysis section is divided into two sections: the first section investigates the cause of inertial motions and analyzes the relationship between wind forcing, state of the sea ice cover, and oceanic inertial oscillations in order to parameterize these characteristics. The second section examines the effects of inertial motions on the base of the ocean mixed layer via analysis of the dynamic stability at the base of the mixed layer. The MLD and estimates of N^2 and shear from IBO observations are used. Once these parameters are found, analysis of Ri at the base of the mixed layer are performed. The data processing procedure used in the second part of the analysis is discussed in the following paragraphs.

Data processing methods used in this study are described using a wind-event case study that produced an inertial response in the sea ice and mixed layer. The primary buoy from which the data is retrieved is AOFB 17-23, located in the eastern Beaufort Sea. Deployed at 81.742°N, 150.879°W, on 04 Aug 2008, AOFB 17 survived the Arctic climate and ice conditions for over two years. Its deployment recently came to an end on 10 Jan 2011, at 81.713°N, 103.108°W. Also deployed on the same ice floe is ITP 23, which was deployed on 05 Aug 2008 at 81° 44.5 N, 150° 53.4 W. This case study

examines YDs 333–340, which corresponds to the winter of 2008. During this time, both the AOFB and ITP buoys are located in the Eastern Beaufort Sea over deep waters where the pycnocline is known to be relatively strong.

2. Determination of the Mixed Layer

Identification and determination of the depth of the Arctic Ocean's mixed layer in data processing is a crucial part of this research, since the focus is the stability at the base of the mixed layer. The first step in our analysis is to identify the base of the mixed layer in order to determine where vertical averaging calculations of shear and N^2 should be made in order calculate the dynamic stability Richardson number at the base of the mixed layer.

The base of the Arctic Ocean mixed layer is determined using a discretized estimation derived from individual density profiles as defined by the following equation $\rho(z_{ml}) = .05\Delta\rho + \rho_{surf}$, where $\Delta\rho = \rho_{60m} - \rho_{surf}$. Here, ρ_{surf} is the density at the first bin of each profile and ρ_{60m} is the density at 60 m. An illustrative view of this equation is depicted in Figure 8. The calculated mixed layer depth, z_{ml}, is then interpolated into 2 hour increments, which allows us to create a time series that will match our AOFB data set as illustrated in Figure 9. After determining the depth of the mixed layer, estimates of the shear and N^2 that will be representative of the base of the mixed layer can be determined.

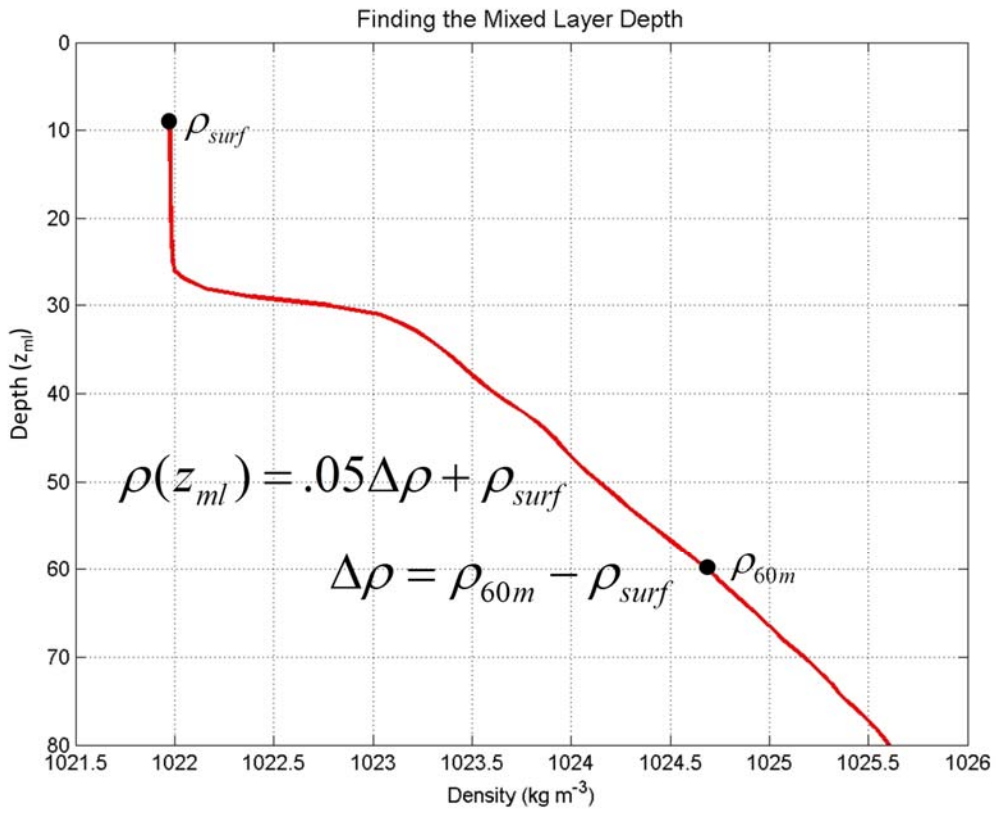

Figure 8. Example density profile illustrating the discretized calculation of the mixed layer depth. ρ_{surf} is the density value of the first data bin of each profile. ρ_{60m} is the density value at 60 m. The change in density is multiplied by a factor of .05 and added to ρ_{surf}. The depth of this summed density value is the depth of the mixed layer.

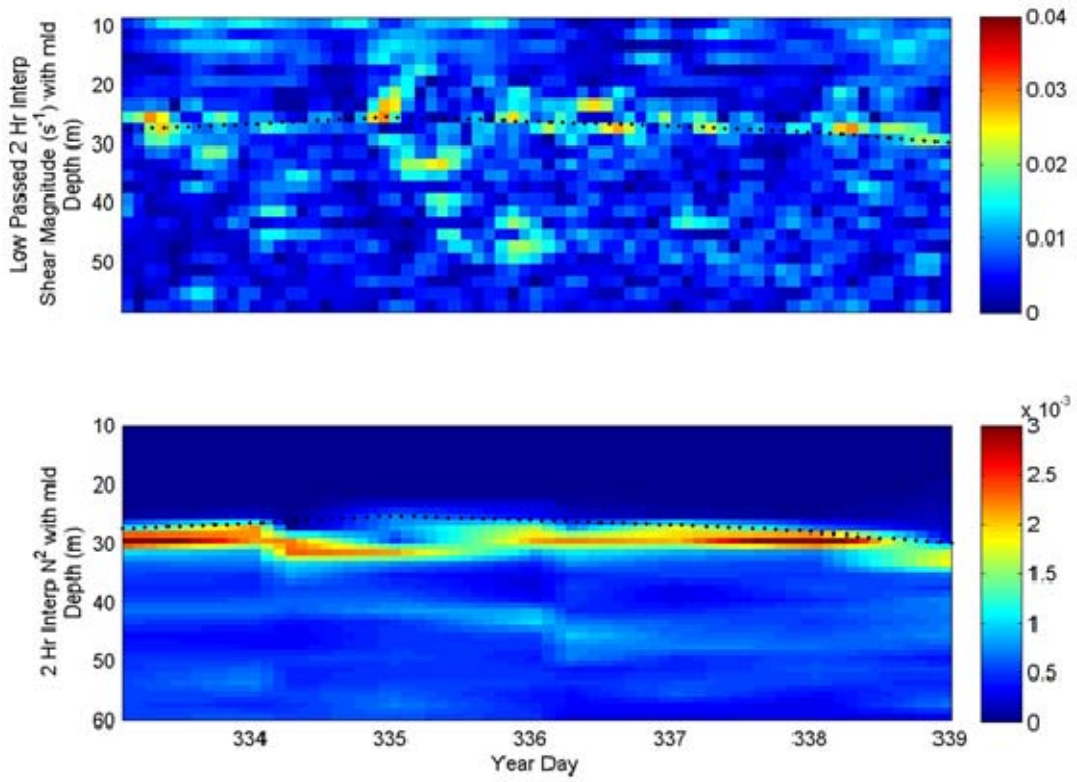

Figure 9. Low-passed shear magnitude as a function of time and depth (top panel) with estimates of the mixed layer depth (black dots). Buoyancy frequency as a function of time and depth (bottom panel) with estimates of the mixed layer depth (black dots). Note how the layers of high shear and stability corrspond well to the estimated depth of the mixed layer.

3. Shear and Extraction of Inertial Velocities

The shear calculated from the original 2 and 4 hour AOFB observations can be seen in Figure 10a. The 2 and 4 hour sampling rate is used to capture inertial velocities. Figure 10b shows the shear calculated from the 2 hour interpolated time series. The frquency content of the 2 hour interpolated time series is initially analyzed using a power denstiy spectrum (Figure 11). From this, the existance of a very large intertial peak at ~11.85 hours with magnitude 0.1947 m/s can be observed along with a much weaker first

harmonic. To isolate the velocities at inertial frequencies, two symetric timeseries low pass filters (with 4'th order cutoffs at 9 hour and 15 hour periods, respectively) are ran on the 2 hour interpolated time series.

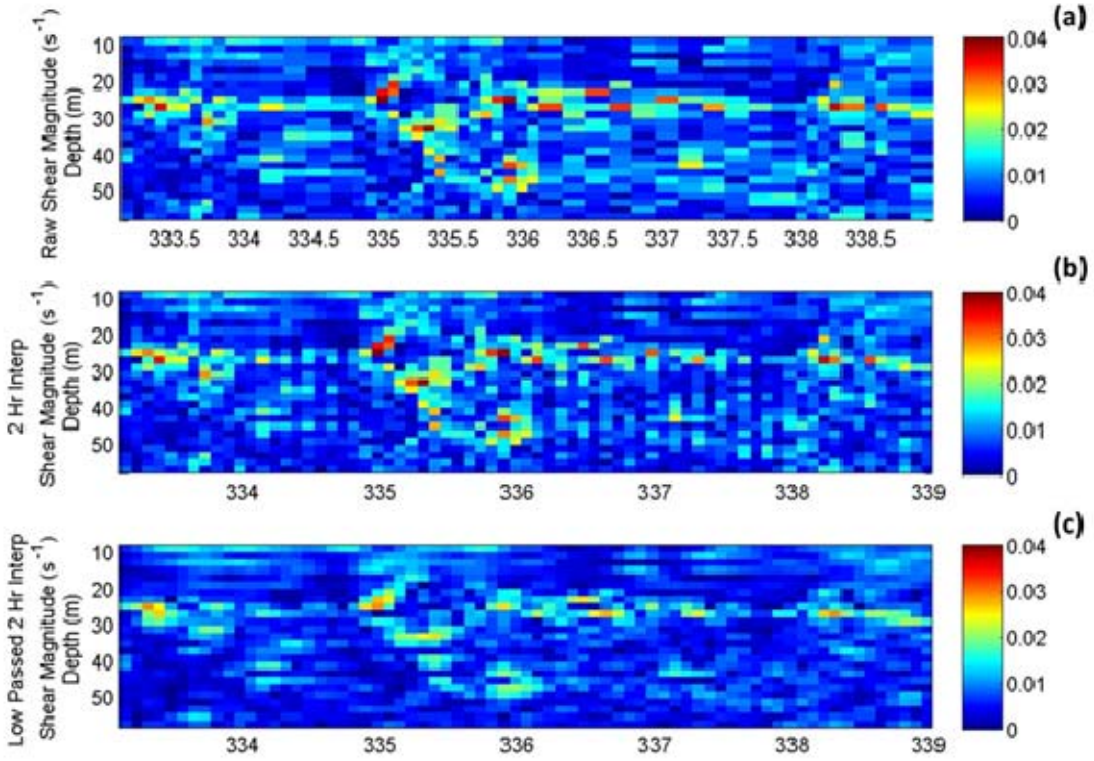

Figure 10. Shear estimates from the AOFB ADCP data. a) Raw, total shear from 2–4 hour observations. b) Raw, total shear from 2-hour-interploated AOFB data. c) Low passed (9 hour) 2-hour-interpolated shear.

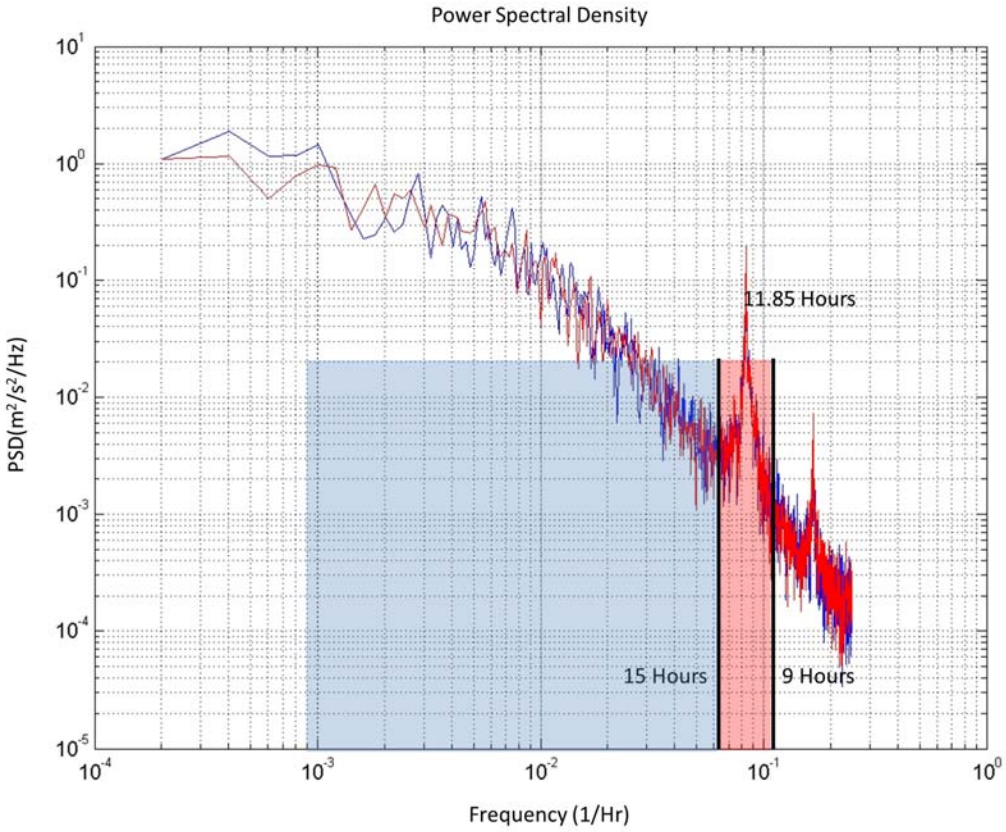

Figure 11. Example spectra of AOFB ADCP, used to determine cutoff times at 9 hours and 15 hour respectively. Inertial frequency band shaded in red. Subinertial frequency band shaded in blue. These two bands sum up to make 'total velocity'.

These filters are ran to isolate inertial and subinertial motions from higher frequency 'geophysical noise' and is completed by using a signal processing method in MATLAB. To start, the time series is overlapped three times in order to reduce the noise and to smooth the signal. Next, a Butterworth filter with a normalized cutoff frequency of 0.4537 (9 hour) is used to produce coefficients for use in 'filtfilt' (MATLAB function). 'Filtfilt' is a zero phase digital filtering function that processes time series data in both forward and reverse directions. Figure 10c shows the shear calculated from the low passed, 2 hour interpolated velocites. This 9 hour period low passed velocity, consisting of inertial and subinertial motions, from here on, is referred to as 'total velocity'. Using similar methods, another low pass filter is ran on the 2 hour interpolated

velocities using a cut off frequency of 0.2715 (15 hour) in order to isolate subinertial velocities. From this, the inertial velocities can be calcuated by subtracting between the 'total velocity' and subinertial velocity. This leaves three variables (better visualized in Figure 11): one with velocities in the inertial and sub-inertial frequency range (called 'total velocity'), the second with velocities in the inertial frequency range, and a third with velocities in the subinertial frequency range.

The magnitude of the shear at the base of the mixed layer can be calculated from these varaibles. This is done in a discretized manner by finding the average vector velocities of the nearest two bins that are above and below the found mixed layer depth. We then find the magnitude of the difference between these average vector velocities. This magnitude is then divided by the depth difference between these bins. The calculation of the magnitude of shear is described by the following formula, and Figure 12.

$$\left\langle \partial \vec{u} / \partial z \right\rangle_{ml} = \frac{\left| \overline{\vec{u}_{z+2} + \vec{u}_{z+1}} - \overline{\vec{u}_{z-2} + \vec{u}_{z-1}} \right|}{\Delta z}$$

Here, $\bar{u}$ represents the 2 hour sampled, filtered u and v components measured by the AOFBs, z represents depth (9–87 m at 2 m increments), and Δz is 6 m. Δz is the distance between the average vector velocities about the found mixed layer depth. The shear derived from the 'total velocity', inertial velocity, and sub-inertial velocity will be used in our calculation of the dynamic stability value of gradient Richardson number.

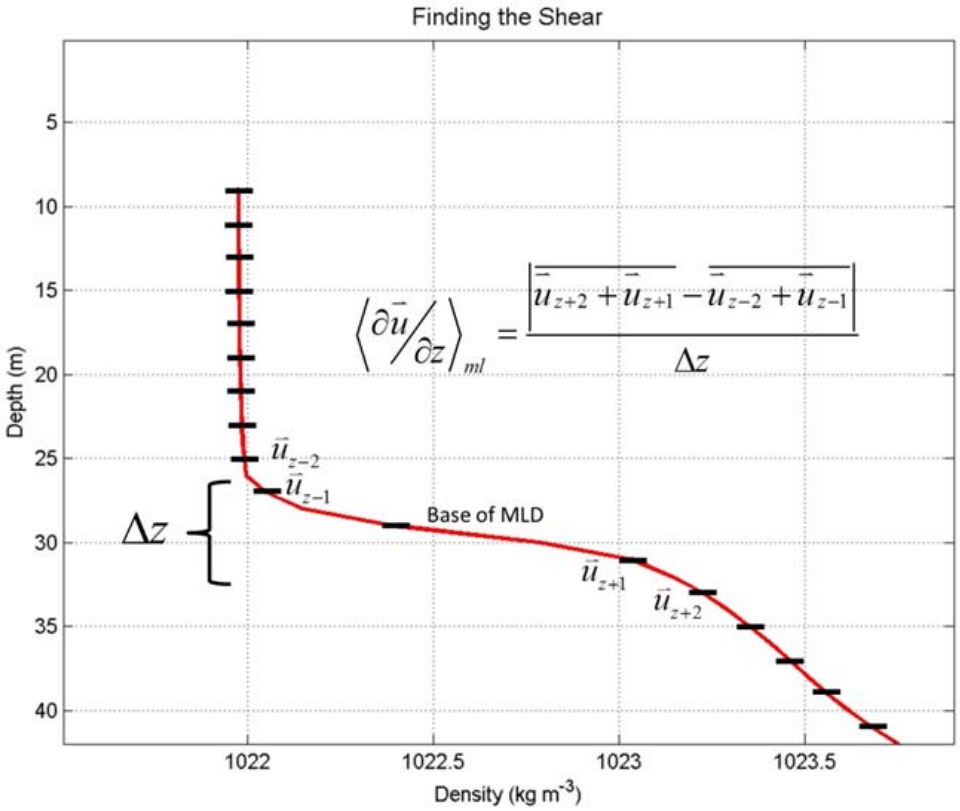

Figure 12. Example density profile to illustrate the discretized calculation of shear at the base of the mixed layer. Here $\bar{u}$ represents the 2 hour interpolated u and v velocity components measured by the AOFBs, z represents depth (9–87 m at 2 m increments), and Δz is 6 m.

4. Calculation of N^2

The Brunt-Vaisala frequency or buoyancy frequency is the frequency at which a parcel will oscillate in a statically stable environment and is described by,

$$N^2 = \left(\frac{g}{\rho}\right)\left(d\rho/dz\right)$$

Here with binned data, g refers to gravity, ρ to density, dρ to the potential density difference between adjacent bins, and dz is 1 m. Profiles of ITP data are made into depth increments of 1 m starting from .5 m to 149.5 m. This allows us to find the value of N^2 in

between adjacent depth measurements, and thus N^2 values from 1 m to 149 m at 1 m increments. Six hour sampled N^2 values are then interpolated to every 2 hours. To find a representative estimate of $\langle N^2 \rangle$ at the base of the mixed layer, and to be consistent with our estimate of shear at the base of the mixed layer, we use the two bin mean difference described above.

5. Gradient Richardson Number

To evaluate the dynamic stability at the base of the mixed layer, and the role of inertial oscillations in particular, we make estimates of shear ('total velocity' and subinertial) and N^2 at the base of the mixed layer. Thus, the value of the Richardson number at the base of the mixed layer for each of these filtered velocities are evaluated as:

$$Ri\ total = \frac{\langle N^2 \rangle}{\left\langle \partial \vec{u} / \partial z \right\rangle^2 (total\ velocity)}$$

$$Ri\ subinertial = \frac{\langle N^2 \rangle}{\left\langle \partial \vec{u} / \partial z \right\rangle^2 (subinertial\ velocity)}$$

For the purposes of the thesis, the inverse of the Richardson number (Ri^{-1}) will be used to better depict this value when plotting, since the stable values of Ri are typically very high and we seek the small values of Ri that reveal instabilities.

III. RESULTS

The results are divided into two sections: section one investigates the cause of inertial motions and analyzes the relationship between wind forcing, state of the sea ice cover, and oceanic inertial oscillations in order to parameterize these characteristics. Section two examines the effects of inertial motions on the dynamic stability at base of the Arctic Ocean mixed layer, and also compares the dynamic stability to satellite derived sea ice concentrations.

A. SECTION ONE

Prior to examining the AOFBs, SSMI and AMSR-E satellite derived ice concentrations, and ERA-Interim winds, each buoy's regional conditions must be examined. Next, the relationship of ECMWF modeled winds to subinertial and inertial sea ice speeds will be examined. Linear regressions between ECMWF modeled winds and normalized subinertial and inertial sea ice speeds during summer (Jul-Sep) and winter (Oct-Dec) will be performed. In order to study the relationship between modeled winds and sea ice speeds, a trend line is fitted on the observational data using the method of least squares - a method that minimizes the sum of the squares of the vertical distance from the trend line to the data points. Finally, the relationship between sea ice inertial speed and sea ice concentration estimates from SSMI and AMSR-E sensors are analyzed.

1. Sea Ice Subinertial and Inertial Velocities and Modeled Winds

a. Canadian Basin

For most of the year, the Canadian Basin is influenced by the constant high pressure system located over the Beaufort Sea. This high pressure system creates an anti-cyclonic turning that influences the flow of the atmosphere and the surface as is determined by a review of the AOFBs' drift tracks. ECMWF's modeled winds show that the average monthly wind magnitude along the AOFBs' drift track remains fairly constant throughout the year, indicating that the inertial oscillations are not modulated by seasonal variations in wind stress in Figure 13.

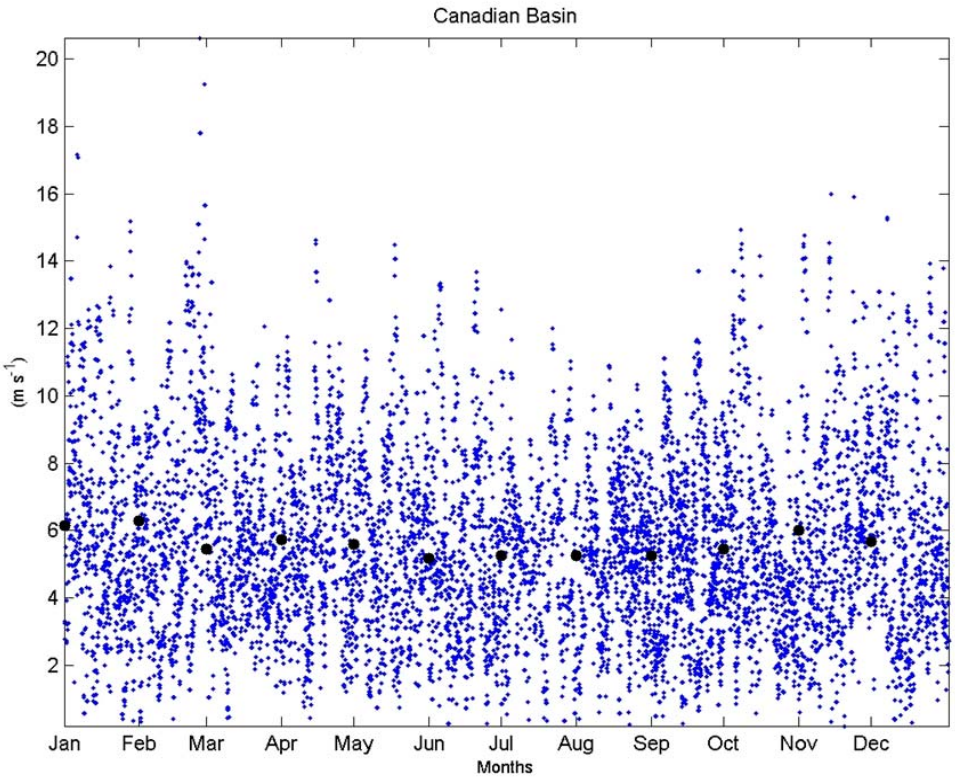

Figure 13. ECMWF wind speeds along the drift tracks of AOFBs 13 and 17, located in the Canadian Basin. (Blue dots represent two hourly wind speeds and black dots are average monthly wind speeds)

Relationships between ECMWF winds and inertial and subinertial sea ice speed responses are different (Figure 14–15). For both summer and winter conditions, as expected, the subinertial sea ice speed and ECMWF modeled winds are correlated (Figure 14). The linear trend for the summer has an $R^2 = 0.3114$, and the linear trend for the winter has an $R^2 = 0.4188$. However, the relationship of summer and winter inertial sea ice speeds to modeled wind speeds have a very weak linear relationship (Figure 15) where the variation in inertial sea ice speed and modeled winds has an $R^2 = 0.0468$ for the summer and $R^2 = 0.0553$ for the winter, showing a very weak, statistically insignificant correlation. This is to be expected since inertial motions are a result of certain types of transient wind forcing, and since the sea ice and mixed layer slab retains their momentum and continues to oscillate once the wind forcing stops, there is unlikely

to be a strong correlation with just wind speed. Both subinertial and inertial sea ice speeds are seen to be greatest during the summer, specifically during August and September (Figure 16), as the low ice concentration conditions in summer time allow for increases in movement of sea ice. Lastly, inertial sea ice speed decreases considerably during winter conditions as can be seen in Figure 15 where sea ice inertial speeds remain weak and roughly at the same magnitude with comparable wind forcing. This is attributed to an increase in ice pack strength, which will be discussed in the following section.

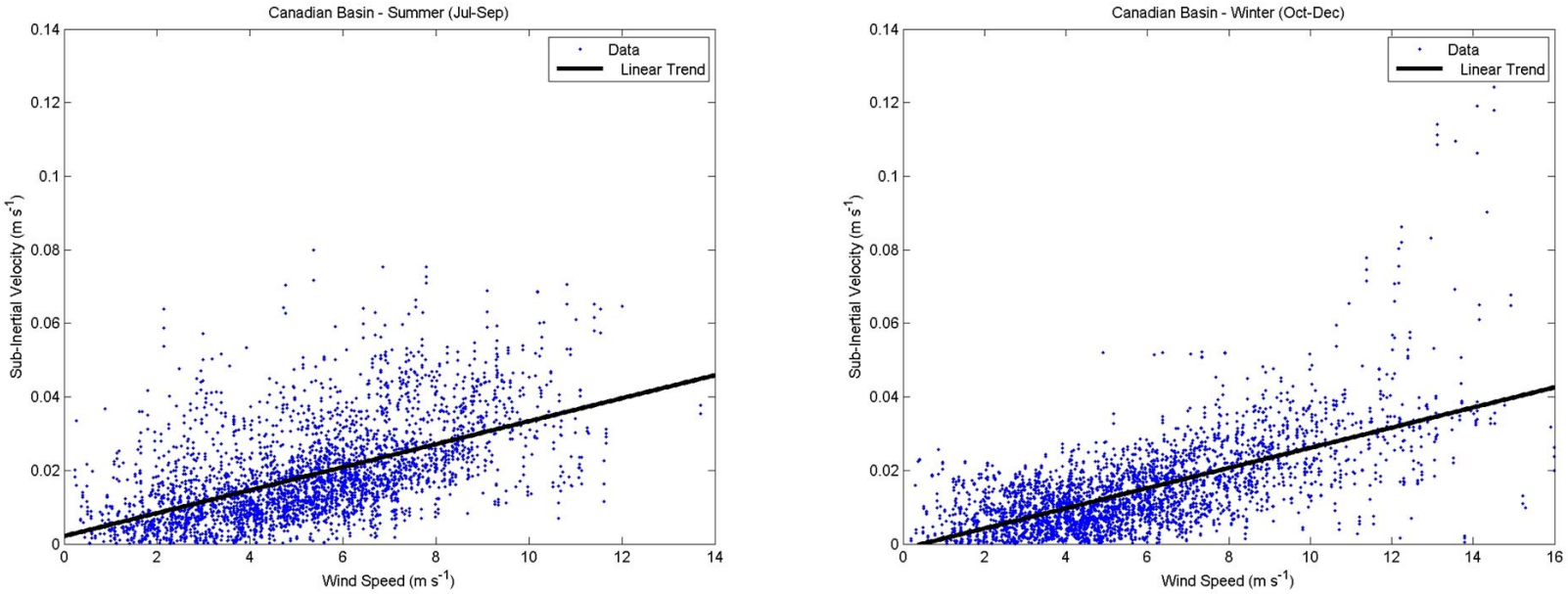

Figure 14. Linear regression between normalized subinertial sea ice speeds from AOFBs 13 and 17 and ECMWF wind speeds. Left panel represents summer time conditions for the months of Jul-Sep. Right panel represents winter time conditions for the months of Oct-Dec.

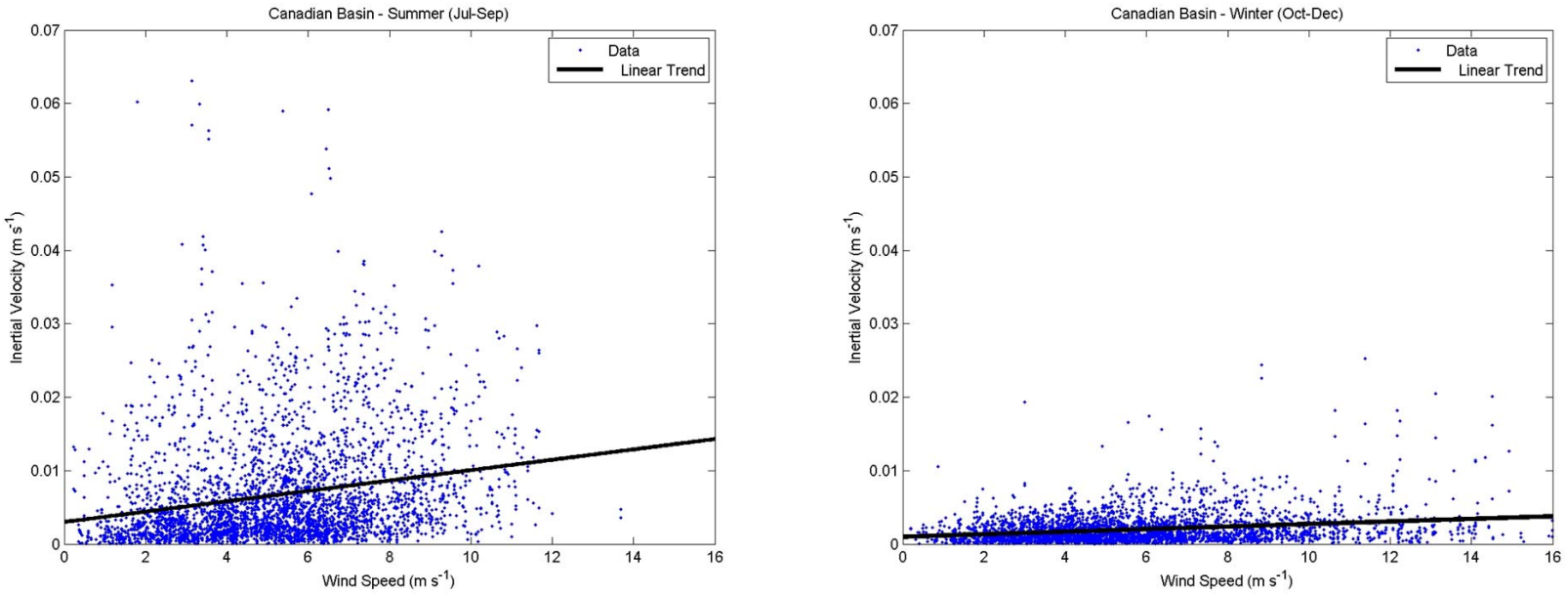

Figure 15. Linear regression between normalized inertial sea ice speeds from AOFBs 13 and 17 and ECMWF wind speeds. Left panel represents summer time conditions for the months of Jul-Sep. Right panel represents winter time conditions for the months of Oct-Dec.

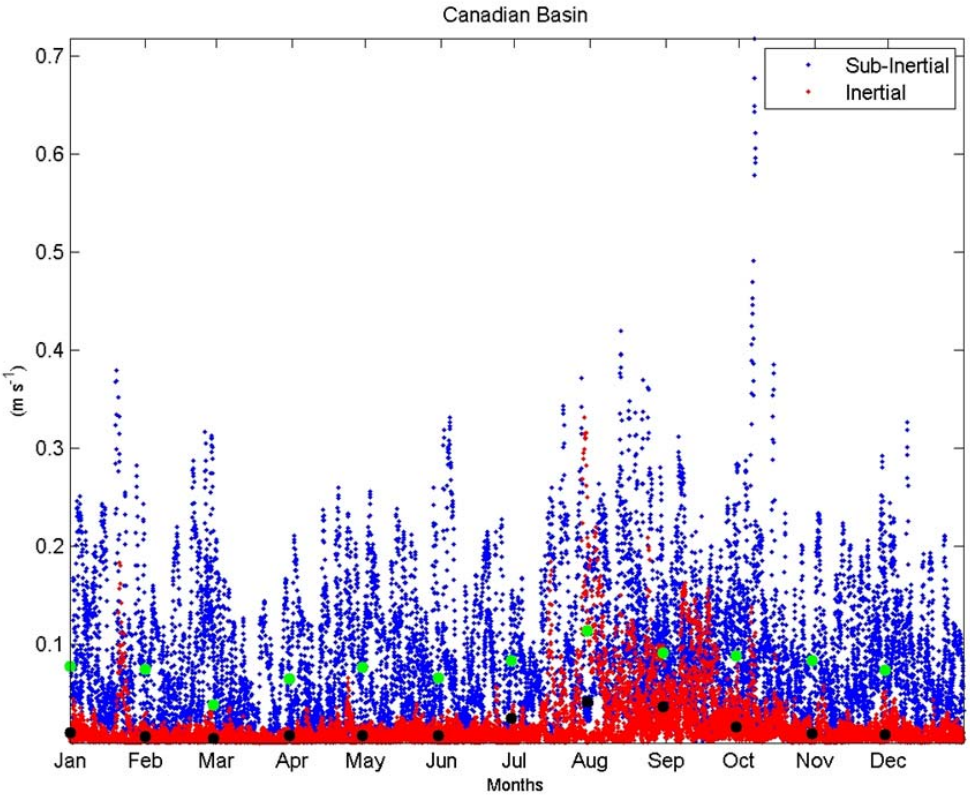

Figure 16. Time series of subinertial and inertial sea ice speeds from AOFBs 13 and 17. Green dots represent average monthly subinertial sea ice velocities and black dots represent average monthly inertial sea ice velocities.

b. Transpolar Drift

When analyzing data sets derived from the Transpolar Drift, spatial and temporal conditions must be considered as the ocean drifts southward from the Eurasian Basin towards the Atlantic Ocean occurs following each spring buoy deployment. For the most of the year, the Transpolar Drift is influenced by the Beaufort Gyre and the Barrents Sea Gyre. The anti-cyclonic and cyclonic turning of these two systems act together to produce a north-south flow over the Transpolar Drift. Results of the ECMWF's wind fields show the average monthly wind speeds and the average wind speeds along the buoy's drift tracks slowly increases towards the end of the year and at lower latitudes as demonstrated in Figure 17.

Similar analyses used for the Canadian Basin are used to evaluate the Transpolar Drift. Similar to conditions in the Canadian Basin, in the Transpolar Drift, correlations between ECMWF winds and inertial and subinertial responses are different (Figure 18–19). For both summer and winter time conditions a linear relationship exists between the variation in subinertial sea ice speed and ECMWF modeled winds (Figure 18) - the linear trend for the summer has an $R^2 = 0.6963$ and linear trend for the winter has an $R^2 = 0.6926$. The correlation of summer and winter inertial sea ice speed to the modeled wind speeds is much smaller and again shows a very weak linear relationship (Figure 19) where the variation in inertial sea ice speed and modeled winds in the summer has an $R^2 = 0.0329$ and $R^2 = 0.1282$ for the winter. The results are similar to those found in the Canadian Basin. Temporally and spatially, both subinertial and inertial sea ice speeds are greatest towards the end of summer and at lower latitudes (Figure 20), as summer time melt and increased distances from the central Arctic allows for increased movements of sea ice along the Transpolar Drift. Lastly, inertial sea ice speed decreases considerably during winter conditions and at higher latitudes where the ice pack strength is the greatest.

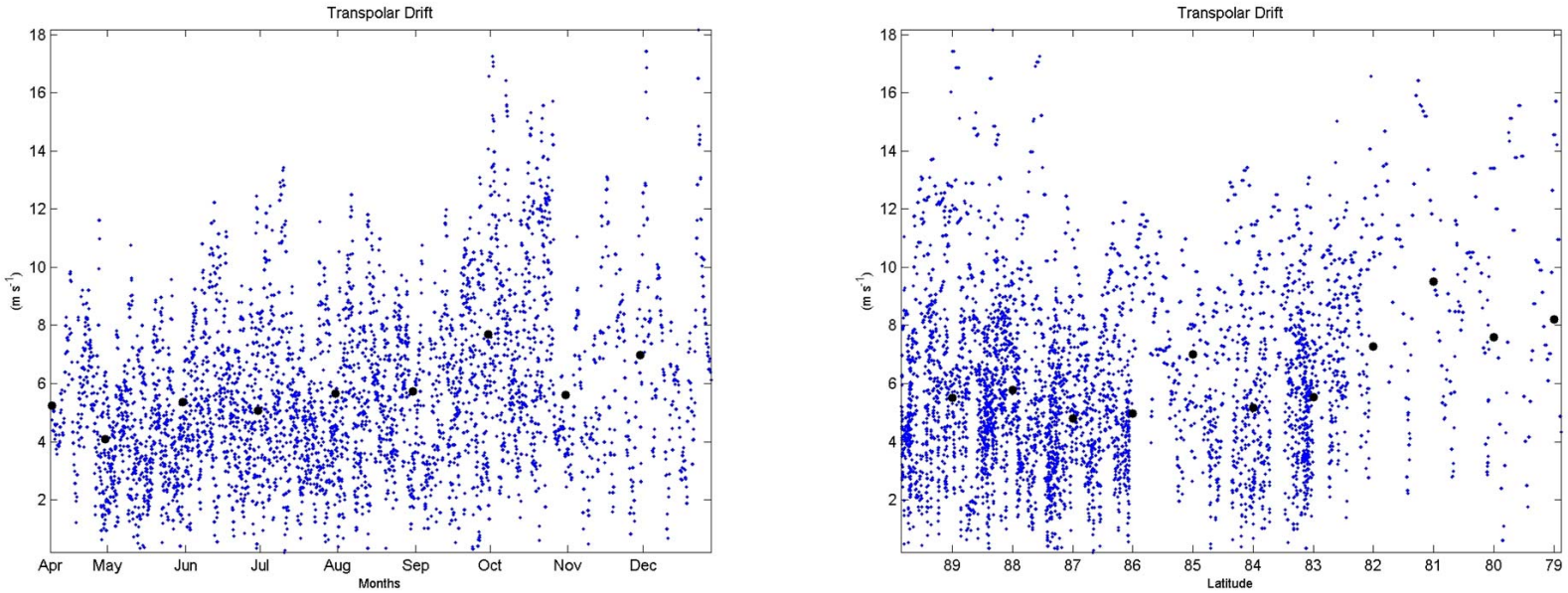

Figure 17. ECMWF wind speeds for AOFBs 11, 14, 15, and 20 located along the Transpolar Drift. Left panel is ECMWF winds as a function of time along drift track. Right panel is ECMWF winds as a function of latitude along drift track. (Blue dots represent two hourly wind speeds and black dots are average monthly wind speeds)

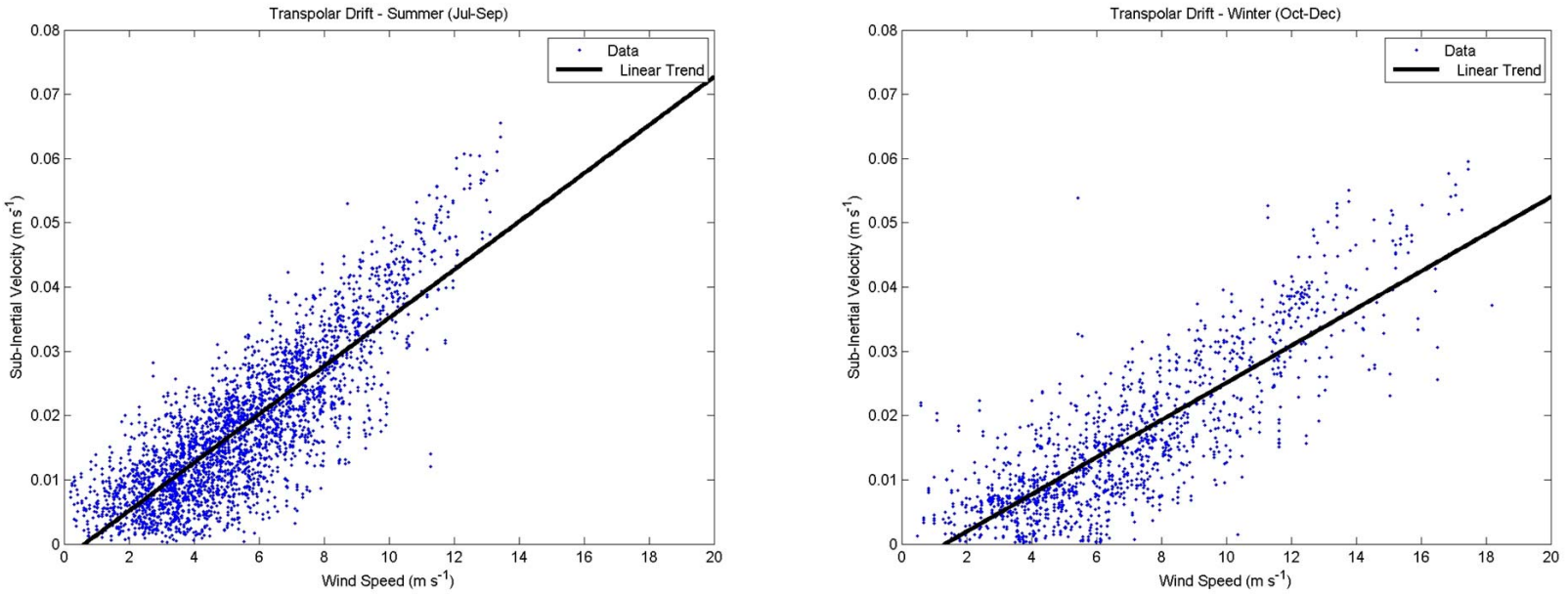

Figure 18. Linear regression between normalized subinertial sea ice speeds from AOFBs 11, 14, 15, and 20 and ECMWF wind speeds for the Transpolar Drift tracks. Left panel represents summer time conditions for the months of Jul-Sep. Right panel represents winter time conditions for the months of Oct-Dec.

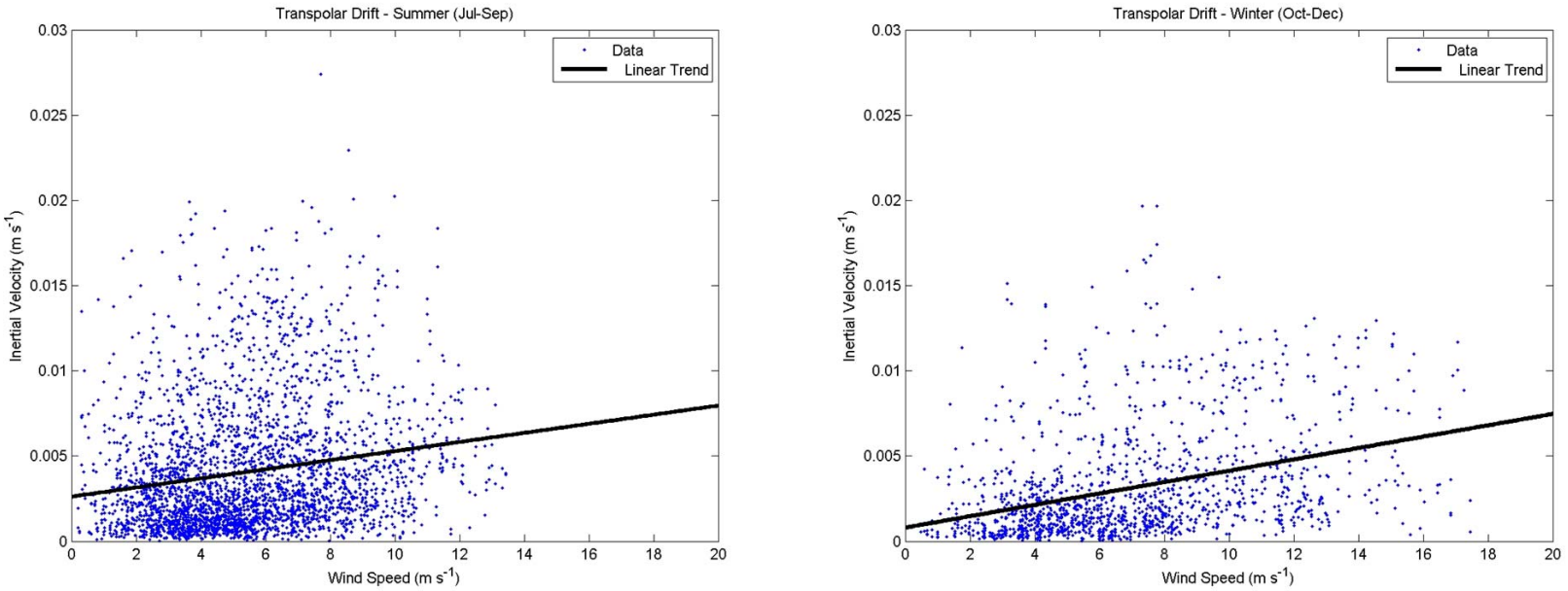

Figure 19. Linear regression between normalized inertial sea ice speeds from AOFBs 11, 14, 15, and 20 and ECMWF wind speeds. Left panel represents summer time conditions for the months of Jul-Sep. Right panel represents winter time conditions for the months of Oct-Dec.

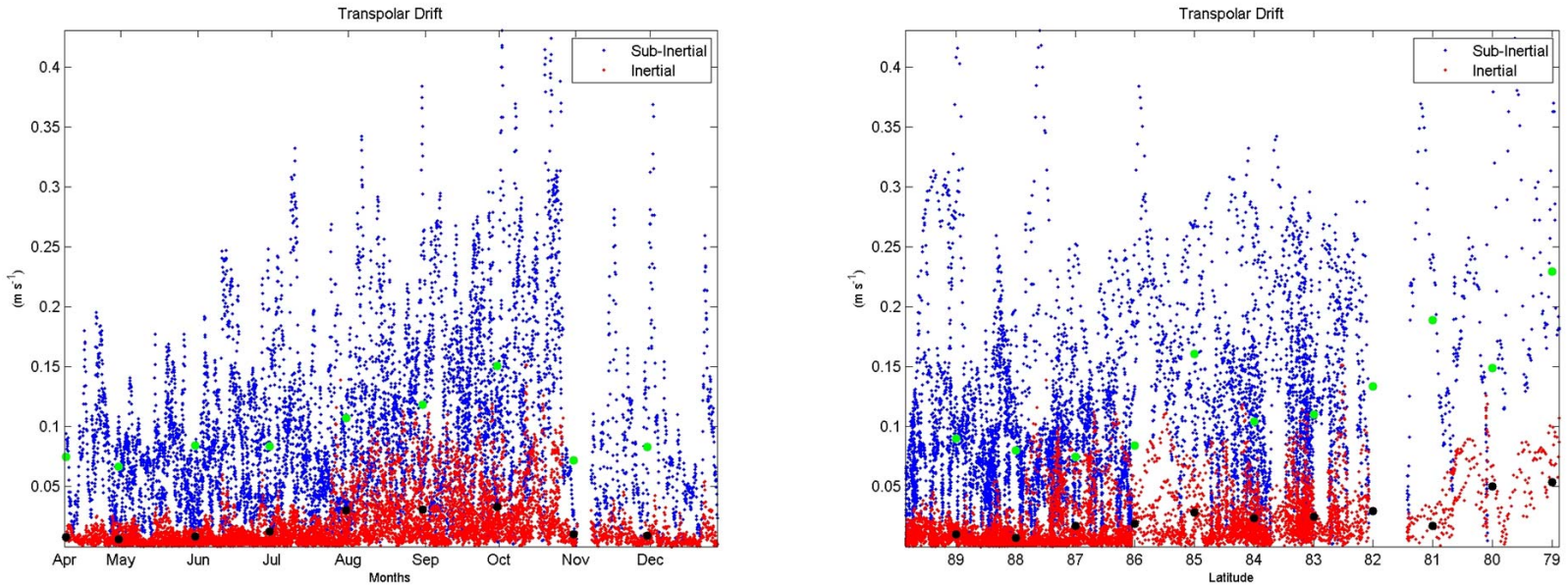

Figure 20. Time and space series of subinertial and inertial sea ice speeds from AOFBs 11, 14, 15, and 20. Green dots represent average monthly subinertial sea ice speeds and black dots represent average monthly inertial sea ice speeds. The large subinertial velocity spike seen on the right panel at latitude 85 is attributed to averaging of sparse data from AOFBs 11 and 20. Both AOFB 11 and 20 were deployed in mid August of 2007 and 2010, respectively.

2. Sea Ice Inertial Velocities and Sea Ice Concentrations

The relationship between sea ice inertial speed and sea ice concentration are investigated by analyzing estimates from SSMI and AMSR-E sensors using AOFB 13 and 17 from the Canadian Basin and AOFB 14 from the Transpolar Drift during part of their summer and winter drifts. Using a scatter plot, the mean sea ice inertial speeds are found at every five percent increments in ice concentration in order to investigate a relationship between sea ice inertial speed and sea ice concentration estimates.

For both AOFBs 14 and 17, sea ice inertial speeds peak during summer months and gradually decline as the Arctic enters the winter season (Figures 21c and 22c). This is to be expected since warmer temperatures support the melting and weakening of sea ice, which in turn establishes an environment where sea ice is able to drift more freely in the ocean. This increased mobility increases the ability for inertial motions to be generated. Conversely, in the presence of increased sea ice concentration during winter, when sea ice is formed and strengthens, the generation of inertial motions is inhibited due to mechanical constraints in the ice motion (Figures 21 c-e and 22 c-e). A scatter plot of both attributes is made (Figures 21 f-g and 22 f-g) that shows that sea ice inertial speeds increase in magnitude as sea ice concentration diminishes. Although we are investigating AOFB data from different years, it can also be seen that the minimum sea ice concentration percentage for the Transpolar Drift does not reach similar levels as that for the Canadian Basin. In both SSMI and AMSR-E sea ice concentration estimates, the sea ice inertial speeds in the Canadian Basin are greater in magnitude when compared to the Transpolar Drift. Similar relationships are seen amongst the rest of the AOFBs until AOFB 13 was analyzed. AOFB 13 is located in the western Beaufort Sea along the marginal ice zone. After comparing AOFB 13's sea ice inertial speed to both SSMI and AMSR-E sea ice concentrations, it is noted that the strong correlation between ice concentration and inertial motion magnitude was not present (Figure 23 c-e). Figure 23 c-e shows that the sea ice inertial speed during days of low sea ice concentration is still large, as the other AOFBs depict, but during days when the sea ice concentration increases, the sea ice inertial speed continues to have a large magnitude. Previously,

other AOFBs depict scenarios that suggest declines in sea ice inertial speeds. This observation can be attributed to the buoy being located in the marginal ice zone in the Beaufort Sea. With the exception of AOFB 13, this analysis determines that parameterization of sea ice inertial speed using sea ice concentration estimates derived from SSMI or AMSR-E satellite sensors is viable.

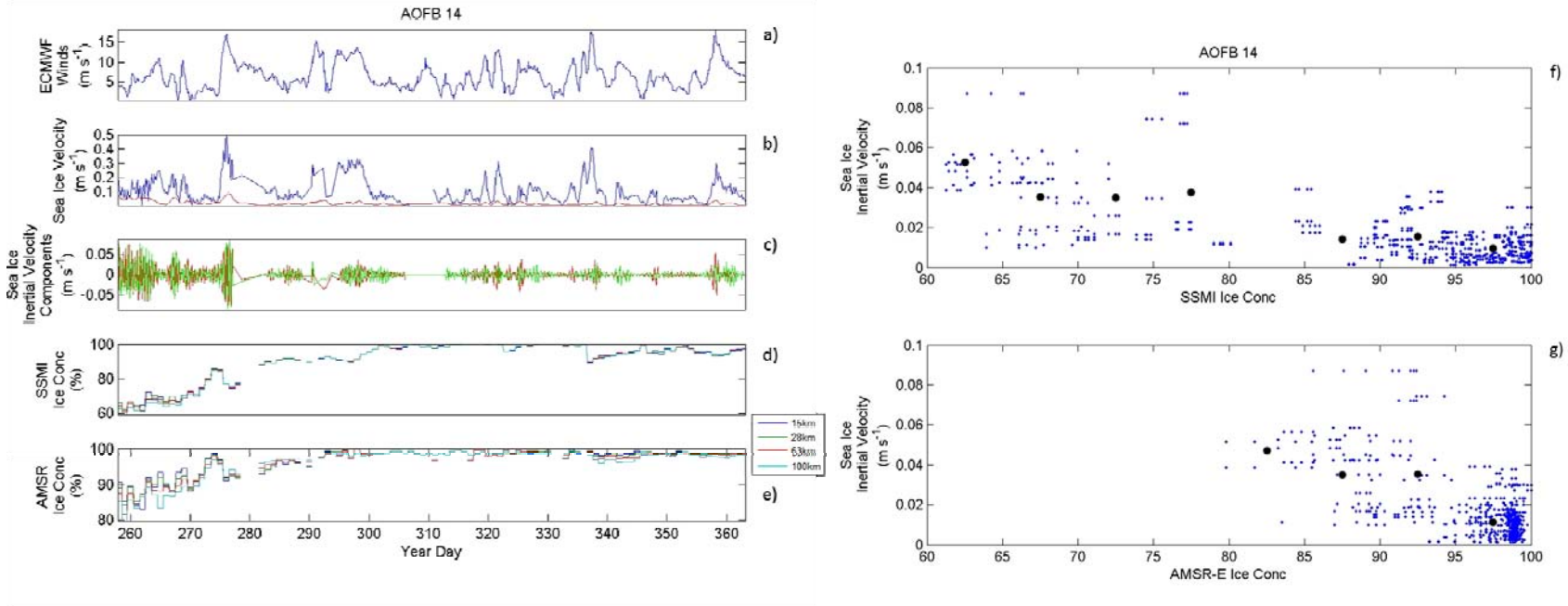

Figure 21. AOFB 14 drift track from YDs 258–365, 2007 a) ECMWF winds b) Sea ice velocity (Total velocity in blue and inertial velocity in red) c) Sea ice inertial velocity (u component in red and v component in green) d) Four estimates of SSMI ice concentrations at 15, 28, 53, and 100 km e) Four estimates of AMSR-E ice concentrations at 15, 28, 53, and 100 km f-g) Scatter plot of sea ice inertial velocity at specific ice concentration (blue dots) with the average sea ice inertial velocity at every five percent ice concentration (black dots).

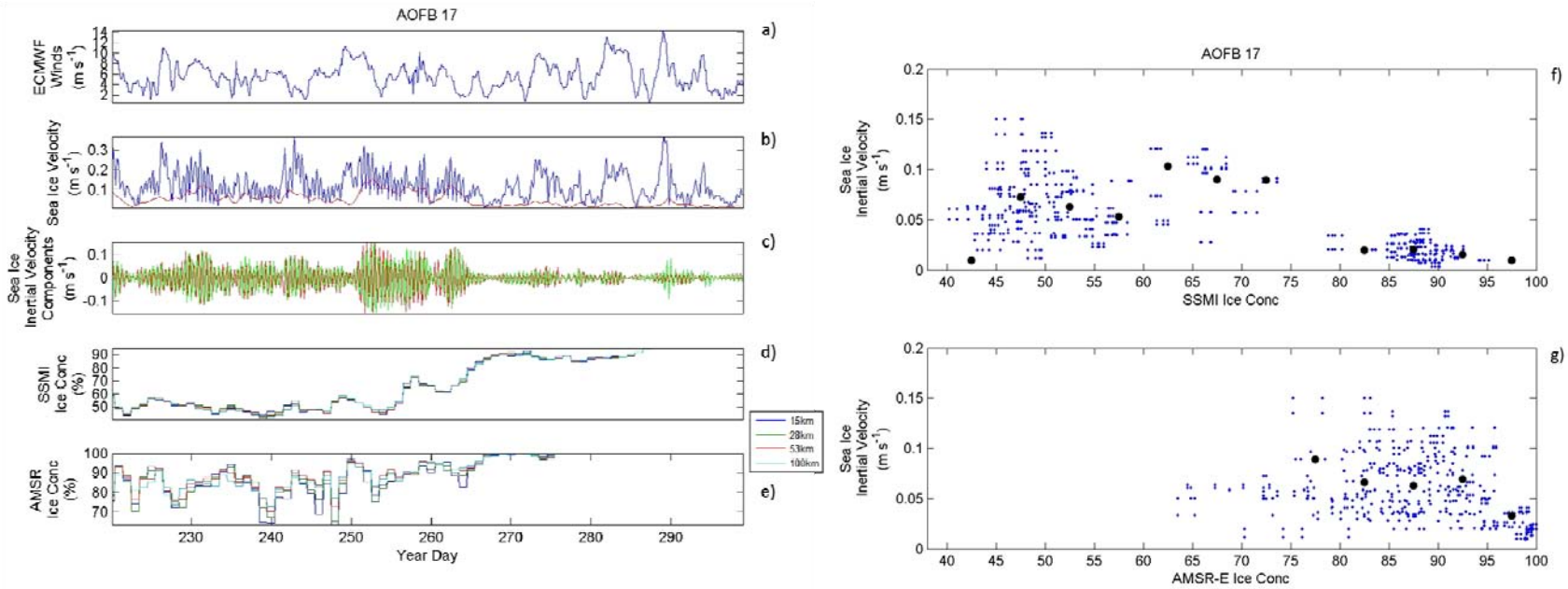

Figure 22. AOFB 17 drift track from YDs 220–300, 2008 a) ECMWF winds b) Sea ice velocity (Total velocity in blue and inertial velocity in red) c) Sea ice inertial velocity (u component in red and v component in green) d) Four estimates of SSMI ice concentrations at 15, 28, 53, and 100 km (note that ice concentration data stops after YD 288) e) Four estimates of AMSR-E ice concentrations at 15, 28, 53, and 100 km (note that ice concetration data stops after YD 276) f-g) Scatter plot of sea ice inertial velocity at specific ice concentration (blue dots) with the average sea ice inertial velocity at every five percent ice concentration (black dots).

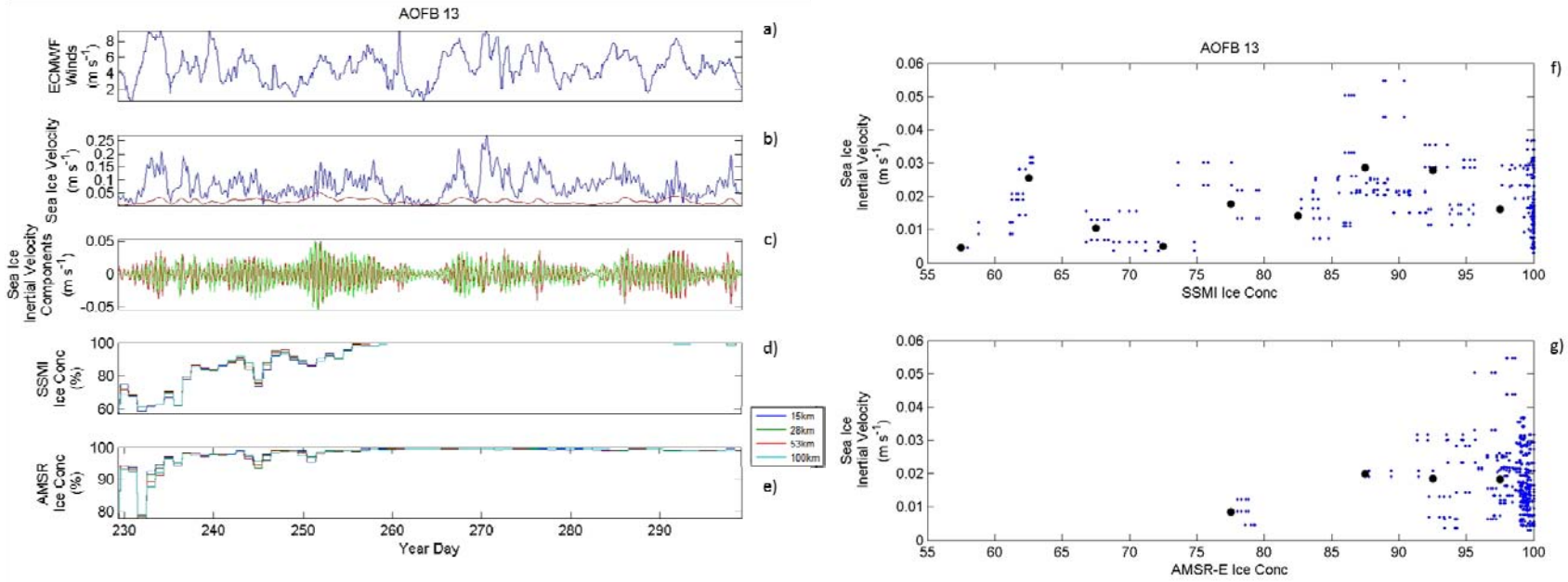

Figure 23. AOFB 13 drift track from YDs 229–300, 2007 a) ECMWF winds b) Sea ice velocity (Total velocity in blue and inertial velocity in red) c) Sea ice inertial velocity (u component in red and v component in green) d) Four estimates of SSMI ice concentrations at 15, 28, 53, and 100 km e) Four estimates of AMSR-E ice concentrations at 15, 28, 53, and 100 km f-g) Scatter plot of sea ice inertial velocity at specific ice concentration (blue dots) with the average sea ice inertial velocity at every five percent ice concentration (black dots).

B. SECTION TWO

The second part of our analysis uses results from IBO observations, ECMWF modeled winds, as well as SSMI and AMSR-E sea ice concentration estimates to investigate the stability of the base of the ocean surface mixed layer to mixing. In the data processing section, a winter time period of IBO 17-23 that was used to describe the methods used for analysis. This winter case study will be contrasted with a summer case study to compare the seasonal variability associated with generating inertial motions and shear at the base of the mixed layer. Analysis will then be expanded to provide a regional comparison between observations gathered in the Transpolar Drift (IBOs 11-7, 14-12, 15-19, and 20-38) and in the Canada Basin (IBOs 13-18 and 17-23).

1. Case Studies

a. Winter Scenario Case Study

During winter, when the ice pack thickens and consolidates, the ability of inertial motions to generate shear or instability at the base of the mixed layer is reduced due to the reduced mobility of the ice pack as depicted in the earlier observations of sea ice speed compared to estimates of sea ice concentrations (Figures 21–22). This event will be investigated using data from IBO 17-23, which is located in the Canadian Basin, west of the Alpha Ridge (Figure 24). During the period of study, this region witnessed a distinct wind-induced inertial event between YDs 334–336 of 2008 (Figure 25b). Analysis of ECMWF winds prior to this inertial impulse shows that five days before the event, winds averaged 7 m/s and reached a maximum speed of 10 m/s (Figure 25a). Figure 25a also depicts a spike of inertial energy from the winds just prior to the sea ice inertial motion. As a result, sea ice reacted with an average inertial speed of ~0.03 m/s, peaking at ~0.05 m/s early on year day 335 (Figure 25b). The winds in the vicinity of IBO 17-23 provides sufficient energy to generate a strong inertial response in the coupled sea ice and mixed layer ‘slab’ during this period.

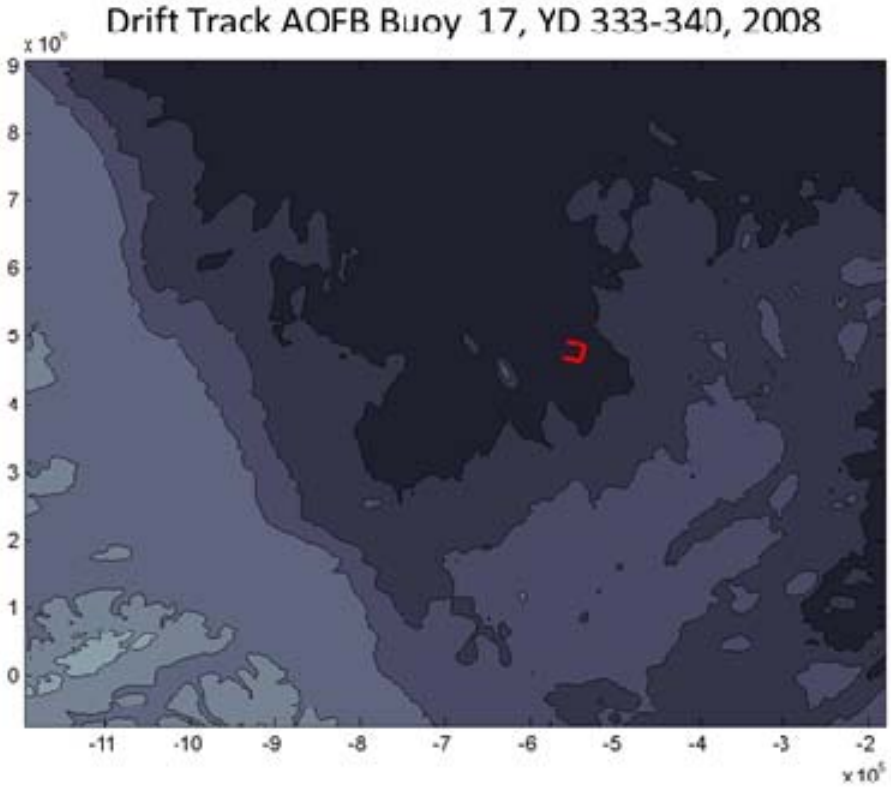

Figure 24. Bathymetric map of Eastern Beaufort Sea with winter case study drift track: IBO 17-23, YD 333–340, 2008.

In order to assess the contribution of inertial shear to instability at the base of the mixed layer, we analyze the subinertial and inertial shear at the base of the mixed layer. An example of reduced dynamic stability can be seen in Figure 25c-g where a weakened density gradient that caused instability at the base of the mixed layer occurred between YD 334–336. During this period, the measured mean inertial shear at the base of the mixed layer (Figure 25e) is ~0.0044 s^{-1} , which is greater than the mean subinertial shear that is ~0.0027 s^{-1}. However, as time passes, the inertial motions decay and the magnitude of the maximum subinertial shear becomes greater than the inertial shear. This suggests that the majority of the energy at the base of the mixed layer consists of inertially generated shear, but the subinertial shear has a quick and strong spike on YD 335. Prior to the observed instability (Figure 25g), the value of N^2 at the base of the mixed layer between YDs 332–334 is strong, measuring ~0.000917 rad s^{-2}, but between

YDs 334 – 336, the value of N^2 decreases, averaging out to ~0.000335 s^{-1} with a maximum value of ~0.000763 rad s^{-2} and minimum value of ~0.0000775 rad s^{-2} (Figure 25d and f). The weakening of the density gradient at the base of the mixed layer prior to YD 334 could be attributed to the mean subinertial shear, which is measured to be stronger than the inertial shear by ~0.0007 s^{-1} between YDs 332–334. This is a very small difference but weakening of the density gradient prior to YD 334 can be attributed to subinertial shear. As a result, this suggests that the early weakening of the density gradient by subinertial shear allows for the combination of subinertial and inertial shear to destabilize the base of the mixed layer between YDs 334–336 (Figure 25g). Further analysis of Figure 25g shows the crucial contribution of inertial energy to the total Ri^{-1} or dynamic instability at the base of the mixed layer. This additional inertial energy cause's inertial shear enhanced turbulent mixing and permits the total Ri^{-1} to exceed the nominal threshold of four, which indicated shear unstable conditions at the base of the mixed layer.

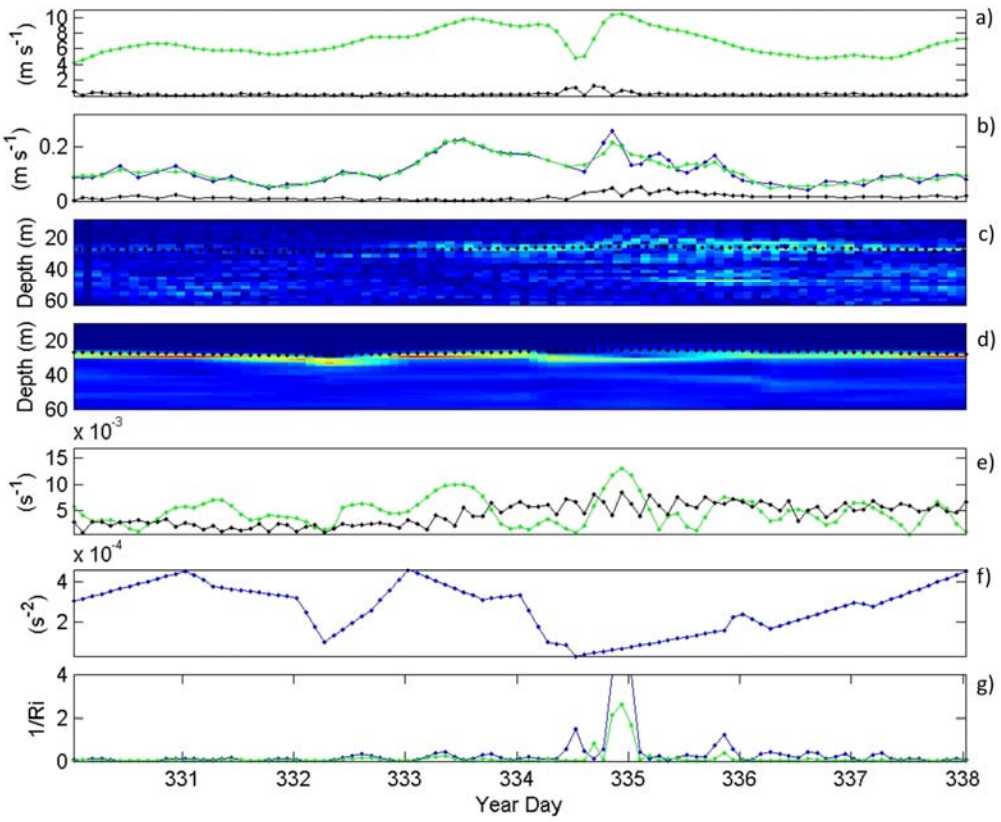

Figure 25. Winter study case. a) ECMWF winds broken down into its subinertial velocity (green line) and inertial velocity (black line) b) Sea ice velocity (Total velocity in blue, subinertial velocity in green, and inertial velocity in black) c) 2 hr interpolated inertial shear (black dots represent the mixed layer) d) 2 hr interpolated N^2 (black dots represent the mixed layer) e) Shear at the base of the mixed layer (subinertial velocity in green and inertial velocity in black) f) N^2 at the base of the mixed layer g) Inverse Richardson number at the base of the mixed layer (Total Ri^{-1} in blue and subinertial Ri^{-1} in green)

b. Summer Scenario Case Study

During summer, the magnitude of inertial motions are expected to increase as depicted in the earlier observations of sea ice speed compared to estimates of sea ice concentrations (Figures 21–22). In order to examine the instability at the base of the mixed layer during summer conditions, the subinertial and inertial energy that is generated at the base of the mixed layer is analyzed. The data sets gathered from IBO

17-23 over a ten day period between YDs 250–260 in mid September are used. At this time, the buoy was located in the Canadian Basin, on the western side of the Alpha Ridge (Figure 26).

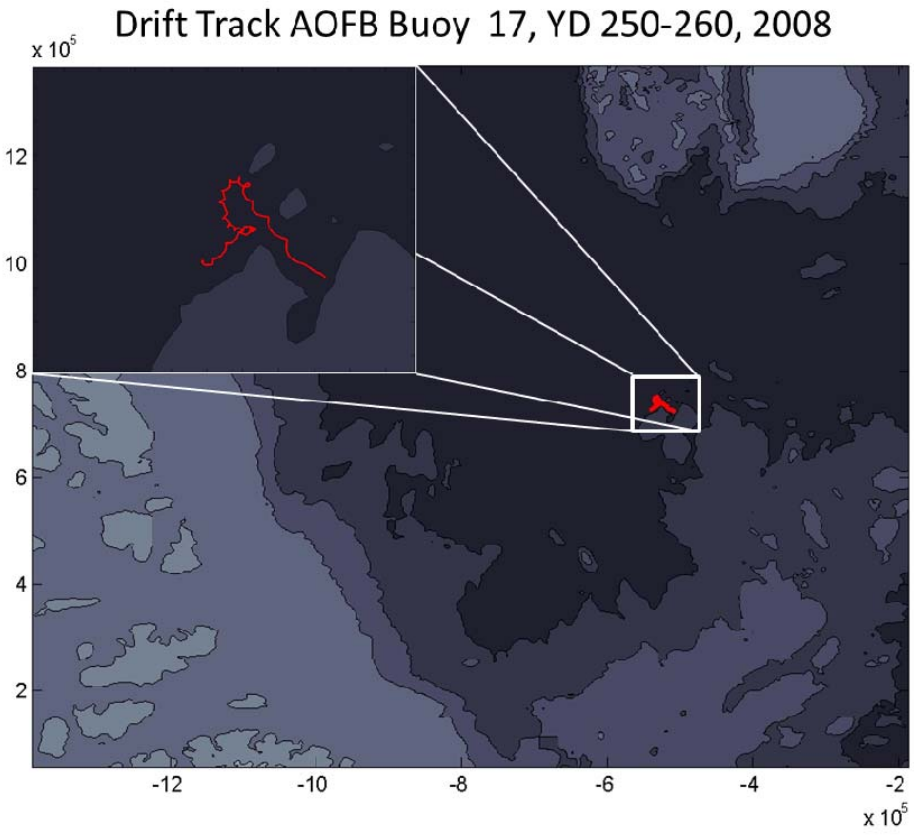

Figure 26. Bathymetric map of Eastern Beaufort Sea with summer case study drift track: IBO 17-23, YDs 250 – 260, 2008.

As a result of the less-compacted sea ice associated with summer conditions (and see section one results), the IBO 17-23 flow reacted to the wind with a large and prolonged inertial response (Figure 27b). Inertial oscillations can be seen in the loops in the buoy's drift track (Figure 26).

These strong inertial motions are attributed to winds. Analysis of ECMWF's winds prior to this lengthy inertial impulse show that five days prior to this event, the five day average wind speed that affected the ice floe was ~8 m/s with peak

winds in this area reaching ~11 m/s (Figure 27a). Sustained winds over the averaged wind speeds of ~8 m/s occurred for roughly two days between YDs 249–251 just prior to the observed burst of inertial energy. Unlike the winter case scenario, inertial wind energy prior to the large sea ice inertial motion is very small (Figure 27a). Thus, it can be established that the winds around IBO 17-23 provides sufficient energy to generate an inertial response in the sea ice between YDs 250–260.

The inertial energy observed in the sea ice motion and coupled ocean mixed layer generates shear at the base of the mixed layer (Figure 27 b-c). On average, the inertial energy at the base of the mixed layer is greater than the subinertial shear (Figure 27c and e). The measured mean inertial shear at the base of the mixed layer for this ten day period is ~0.0059 s^{-1} reaching a maximum of ~0.0122 s^{-1}. The corresponding mean subinertial shear is measured to be ~0.0030 s^{-1} and peaked at ~0.0114 s^{-1}.

The large spike in inertial energy recorded between YDs 252–254 causes unstable shear stability and likely enhanced turbulent mixing at the base of the mixed layer (Figure 27g). The observed inertial shear enhanced instability is supported by the magnitude of inertial shear rather than a change or weakening in the density gradient at the base of the mixed layer. The measured mean inertial shear between YDs 252–254 is ~0.008 s^{-1} , which is larger than the subinertial shear that is ~0.0037 s^{-1}. The density gradient, prior to and during the instability did not change as greatly as it did during the winter case study (Figure 27d and f). Prior to YD 252, the density gradient between YDs 248–252 is ~0.000447 rad s^{-2}. Between YDs 252–254, the density gradient is ~0.000408 rad s^{-2}. From this it can be deduced that the inertial motion of freer ice floe and ocean mixed layer creates a stronger inertial shear level compared to subinertial shear (Figure 27g).

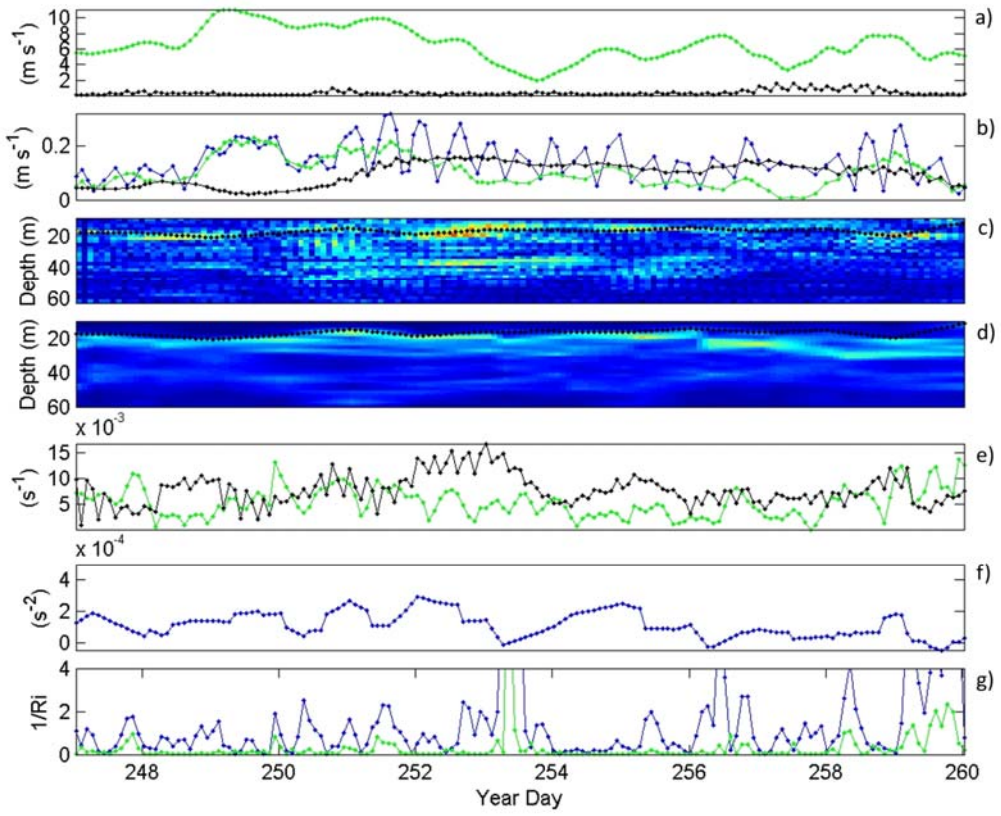

Figure 27. Summer case study. a) ECMWF winds broken down into its subinertial velocity (green line) and inertial velocity (black line) b) Sea ice velocity (Total velocity in blue, subinertial velocity in green, and inertial velocity in black) c) 2 hr interpolated inertial shear (black dots represent the mixed layer) d) 2 hr interpolated N^2 (black dots represent the mixed layer) e) Shear at the base of the mixed layer (subinertial velocity in green and inertial velocity in black) f) N^2 at the base of the mixed layer g) Inverse Richardson number at the base of the mixed layer (Total Ri^{-1} in blue and subinertial Ri^{-1} in green)

2. Regional study

Data sets analyzed from buoys regionally located in the Canadian Basin (IBOs 13-18 and 17-23) and the Transpolar Drift (IBOs 11-7, 14-12, 15-19, and 20-38) will be discussed in this section. These regions are analyzed separately because they are governed by different atmospheric and oceanographic influences. Thus, development of shear and instability at the base of the mixed layer are affected differently in each region

and during different seasons. First we will examine when inertial shear is greatest compared to subinertial shear and if there is any relationship between this and stratification at the base of the mixed layer. We then examine the probability of inertially generated shear enhanced turbulent mixing throughout the year. Finally, we compare inertially produced dynamic instability (Ri^{-1} Inert > 2) at the base of the mixed layer to SSMI and AMSR-E derived sea ice concentration estimates.

a. Canadian Basin

The shear and stability at the base of the mixed layer generated in the Canadian Basin is driven by several seasonal elements unique to the region. One such element is a constant high pressure system over the Beaufort Sea, which influences the winds, ocean, and sea ice. This anti-cyclonic circulation of the ocean and ice is known as the Beaufort Gyre. Other factors include seasonal stratification that is affected by freshwater introduced from river runoff, ice melt, and the Pacific Ocean.

It is hypothesized that the stability at the base of the mixed layer is modulated by sea ice concentration. Timing of inertial shear and sub inertial shear at the base of the mixed layer follows the same temporal pattern as sea ice motion (left panels of Figure 20 and 28). An analysis of inertial sea ice speed determines that the speed is greatest during the months of August and September and smallest during winter months (Figure 16). Figure 28 (left panel) depicts a similar temporal pattern where inertial shear and subinertial shear at the base of the mixed layer have large magnitudes in mid to late summer. However, the ratio of inertial shear to subinertial shear at the base of the mixed layer depicts a different situation. Figure 28 (right panel) shows that the ratio is greatest during the months of June and July. This does not coincide with the time period during which we see the greatest sea ice speed - the months of August and September. The reason for which the ratio is higher earlier in the season is unclear. A physical explanation does not exist other than suggestions inferred via analysis of AOFB 13 data (section one results) where large inertial motions were observed during periods of high ice concentration estimates.

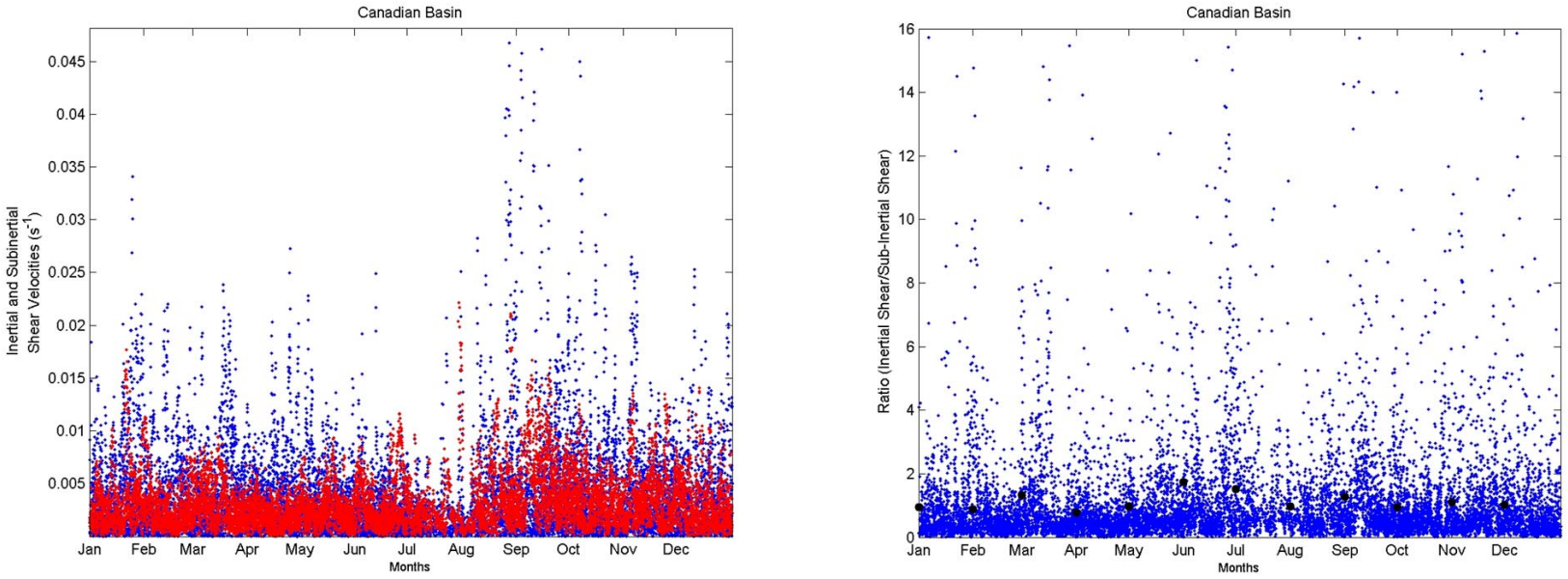

Figure 28. Time series of the inertial shear and subinertial shear measured at the base of the mixed layer (left panel). Time series of the ratio between inertial shear and subinertial shear measured at the base of the mixed layer (right panel). Black dots represent average monthly values.

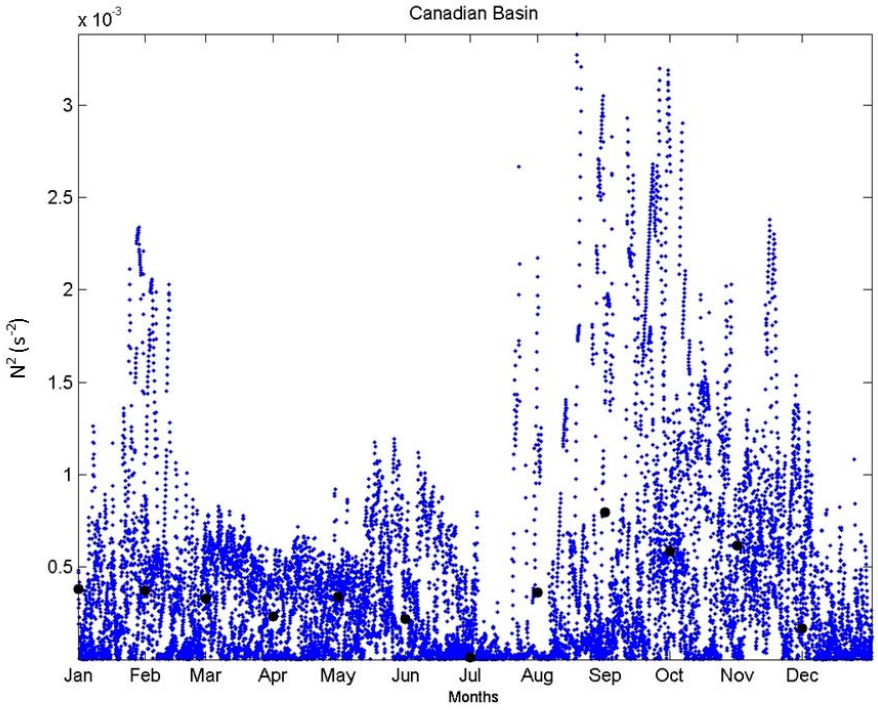

Figure 29. Time series of N^2 measured at the base of the mixed layer. Black dots represent average monthly values.

We now examine the seasonality of the stratification at the base of mixed layer (Figure 29) where it is observed that N^2 gets stronger during mid to late summer due to fresh water input from ice melt water and becomes weaker as the months progress into winter due to freezing of sea ice.

We now determine the frequency of dynamic instability (quantified by Ri^{-1} total > 2) at the base of the mixed layer is supported by inertial motions. It is hypothesized that occurrences of $Ri^{-1} > 2$ would occur greatest during summer when the possibility of generating inertial motions is greatest due to freer sea ice. Monthly fractional occurrences of $Ri^{-1} > 2$ are shown in Figure 30 and Table 1. The largest occurrence of $Ri^{-1} > 2$ is observed to occur during April, June, July, and December. The majority of these months coincide with periods where increases in the ratio of inertial to subinertial shear velocities and decreases in stratification occur at the base of the mixed

layer. During summer months, (Jul-Sep) 12% of occurrences of ‘Ri Total’ would not occur unless supported by inertial shear velocities. Compared to winter months (Oct-Dec) there is not a significant difference in these occurrences where ‘Ri Total’ needs the support of inertial shear velocities 11% of the time. The probability of observing ‘Ri Total’ in either season is about equal, ~58% in summer and ~57% in winter. The probability of ‘Ri Inertial’ occurring is greatest during summer with a probability of ~21% versus ~14% in winter. And the probability of ‘Ri Sub-Inertial’ occurring is greatest during winter with a probability of ~30% versus ~21% in summer. In the Canadian Basin, it is observed that inertial shear supports ‘Ri^{-1} total’ the most during summer months, whereas subinertial shear contributes the most during winter. However, there is one example in the data where in December there is a large spike in ‘Ri inertial,’ which is most likely associated with the weak stratification observed for that month (Figure 29).

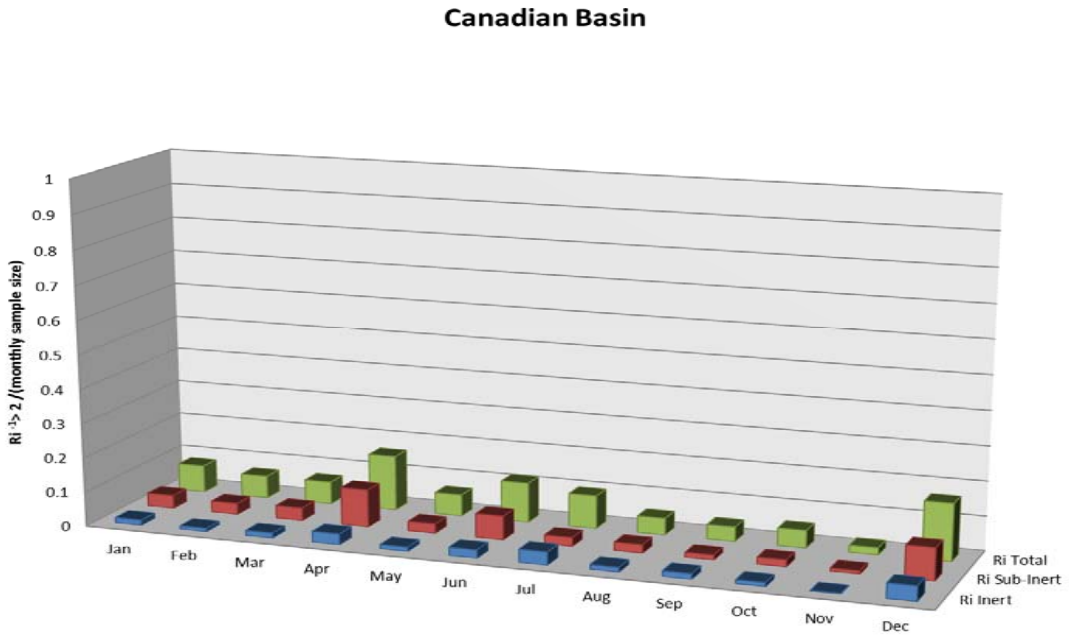

Figure 30. Monthly fractional occurrence of $Ri^{-1} > 2$ for the Canadian Basin. ('Ri Total' calculated from subinertial and inertial velocities in green. 'Ri Sub-Inert' calculated from subinertial velocities in red. 'Ri Inert' calculated from inertial velocities in blue.)

	Jan	Feb	Mar	Apr	May	Jun	Jul	Aug	Sep	Oct	Nov	Dec
RiInert	0.0156	0.0099	0.0152	0.0315	0.0125	0.0241	0.038	0.0138	0.016	0.0116	0.0019	0.0435
Ri Sub-Inertial	0.0384	0.0327	0.0376	0.1093	0.0278	0.0694	0.0261	0.0244	0.0146	0.0206	0.0093	0.0939
Ri Total	0.0796	0.0655	0.0654	0.1602	0.0627	0.1157	0.0962	0.0487	0.0424	0.0512	0.0204	0.1661

Table 1. Values for monthly fractional occurrence of $Ri^{-1} > 2$ for the Canadian Basin.

The inertial motion enhanced dynamic instability (quantified by ‘Ri Inert’ > 2) at the base of the mixed layer is now compared to SSMI and AMSR-E derived ice concentration estimates in the Canadian Basin to investigate whether or not the dynamic stability at the base of the mixed layer can be related to satellite derived sea ice concentration estimates.

It is hypothesized that ‘Ri Inert’ > 2 will increase with decreasing satellite derived sea ice concentrations. Analysis of Figure 31 indicates a clear relationship between ‘Ri Inert’ and SSMI and AMSR-E sea ice concentrations does not exist. Similar observations are seen for ‘Ri Total’ and ‘Ri Sub-Inert’. In Section 1, we found a tentative relationship between sea ice inertial motions and ice concentrations. Because mixed layer base stability is also dependent upon stratification, it is not surprising that the stability has no clear relationship to ice concentration.

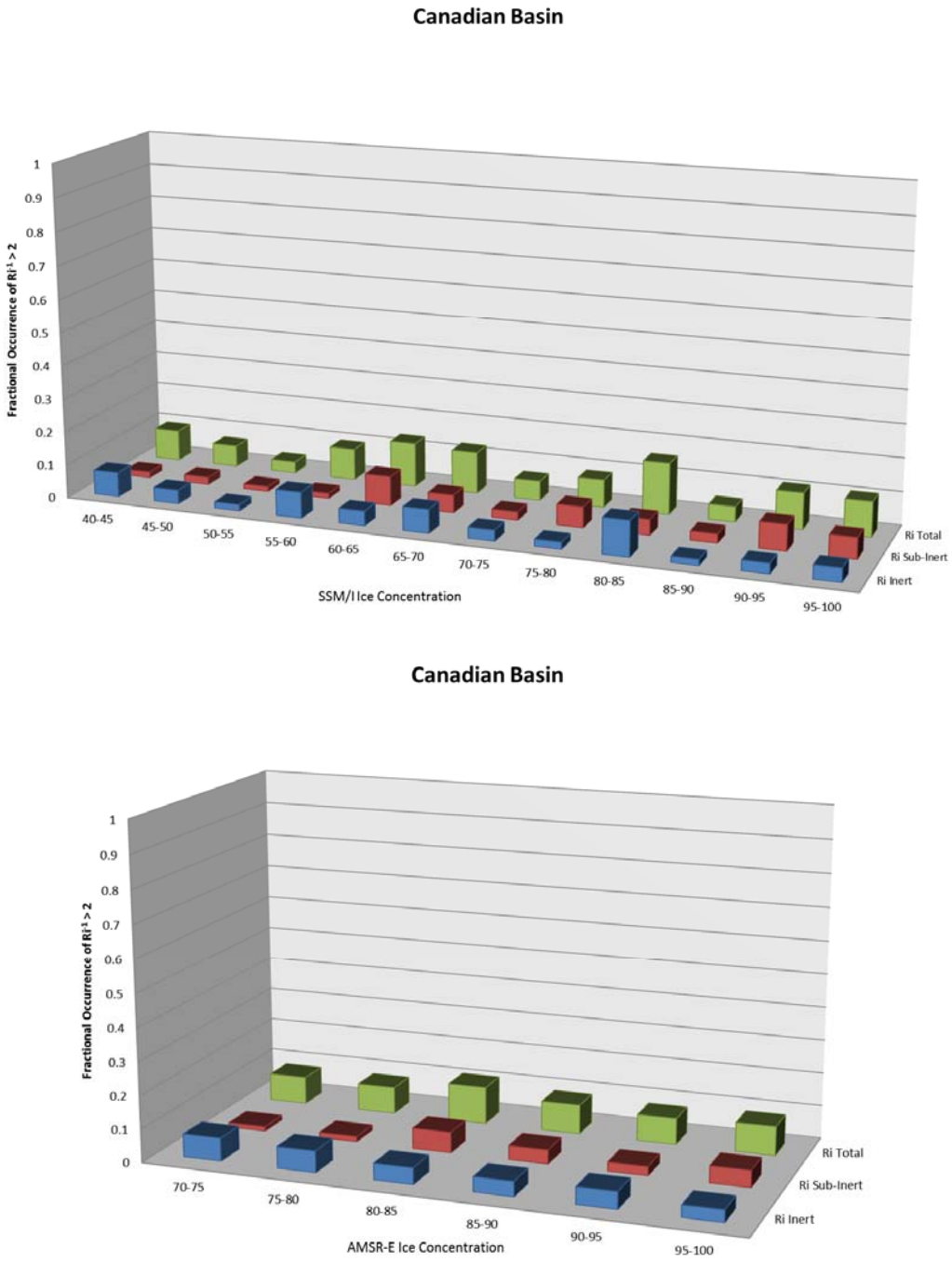

Figure 31. Top panel: $Ri^{-1} > 2$ compared to SSMI sea ice concetrations for the Canadian Basin. Bottom panel: $Ri^{-1} > 2$ compared to AMSR-E sea ice concetrations for the Canadian Basin. ('Ri Total' calculated from subinertial and inertial velocities in green. 'Ri Sub-Inert' calculated from subinertial velocities in red. 'Ri Inert' calculated from inertial velocities in blue)

b. Transpolar Drift

The shear and stability at the base of the mixed layer generated along the Transpolar Drift are driven by large scale atmospheric patterns that force the ice southward between Greenland and Svalbard. Freshwater introduced from river runoffs, ice melt produces seasonal variability in stratification. In-situ measurements of these attributes are gathered by IBOs 11-7, 14-12, 15-19, and 20-38. When analyzing data sets from these buoys, the mix of spatial and temporal changes must be considered as the buoys traverse and drift southward from the Eurasian Basin towards the Atlantic Ocean during the course of each summer.

Again, it is hypothesized that the stability at the base of the mixed layer is modulated by sea ice concentration. Temporally, just as it is for the Canadian Basin, the timing of inertial shear and sub inertial shear at the base of the mixed layer follows the same temporal pattern as the sea ice motion in the Transpolar Drift. (left panels of Figure 20 and 32). Spatially, it is difficult to determine a relationship between the two (Figure 20 right panel and Figure 33 left panel). Our initial temporal analysis of sea ice inertial speed shows that these magnitudes are greatest towards the end of summer, specifically during the month of October, and weakens in the months that follow. However, (Figure 32 right panel) the ratio of inertial to subinertial shear at the base of the mixed layer is largest progressively from July to August. As is the case for the Canadian Basin, this period does not coincide with when we see the largest sea ice speed and the reason for the higher ratios earlier in the season is unclear. Spatially, sea ice inertial speed increases at lower latitudes, which is consistent with the observed ratio of inertial to subinertial shear at the base of the mixed layer, which also increases towards lower latitudes, but drops off after 81° (Figure 33).

We now examine the seasonality of the stratification at the base of the mixed layer (Figure 34). Temporally, the Transpolar Drift experiences similar results to the Canadian Basin. Spatially, N^2 becomes weaker as the buoys approach lower latitudes and drifts closer to the Nordic Seas and the Atlantic Ocean, away from fresh water inputs.

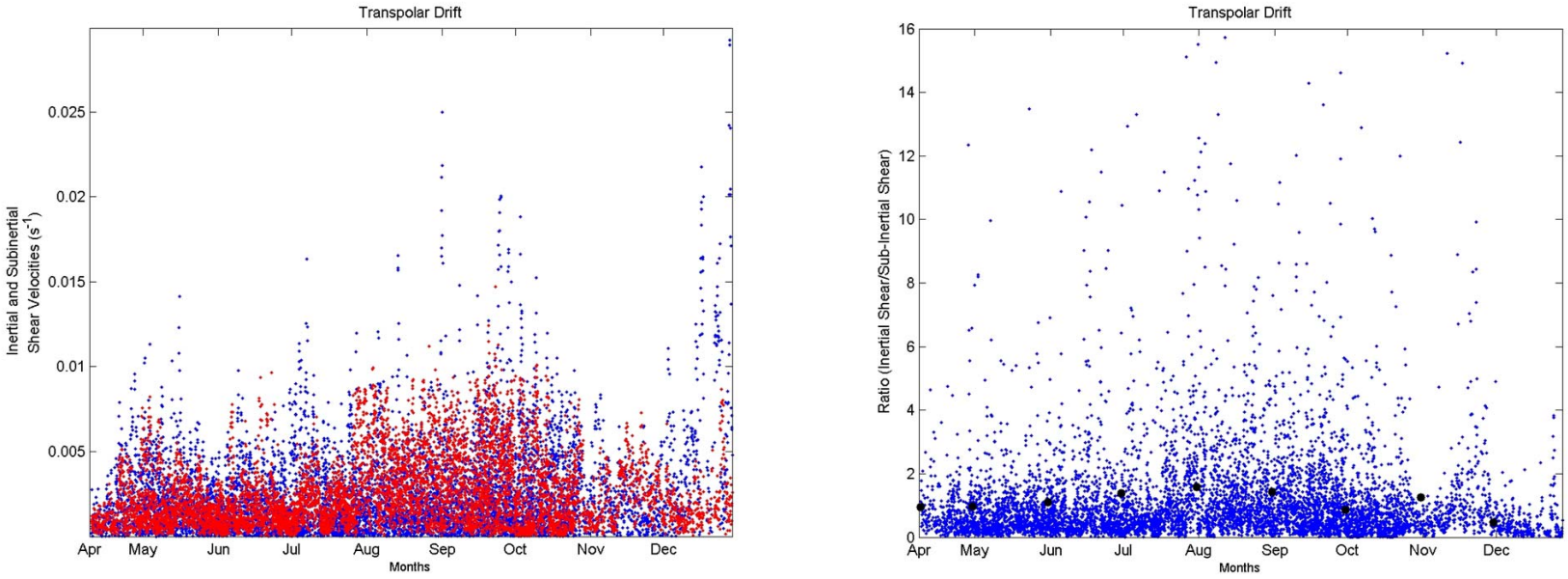

Figure 32. Time series of the inertial shear and subinertial shear measured at the base of the mixed layer (left panel). Time series of the ratio between inertial shear and subinertial shear measured at the base of the mixed layer (right panel). Black dots represent average monthly values.

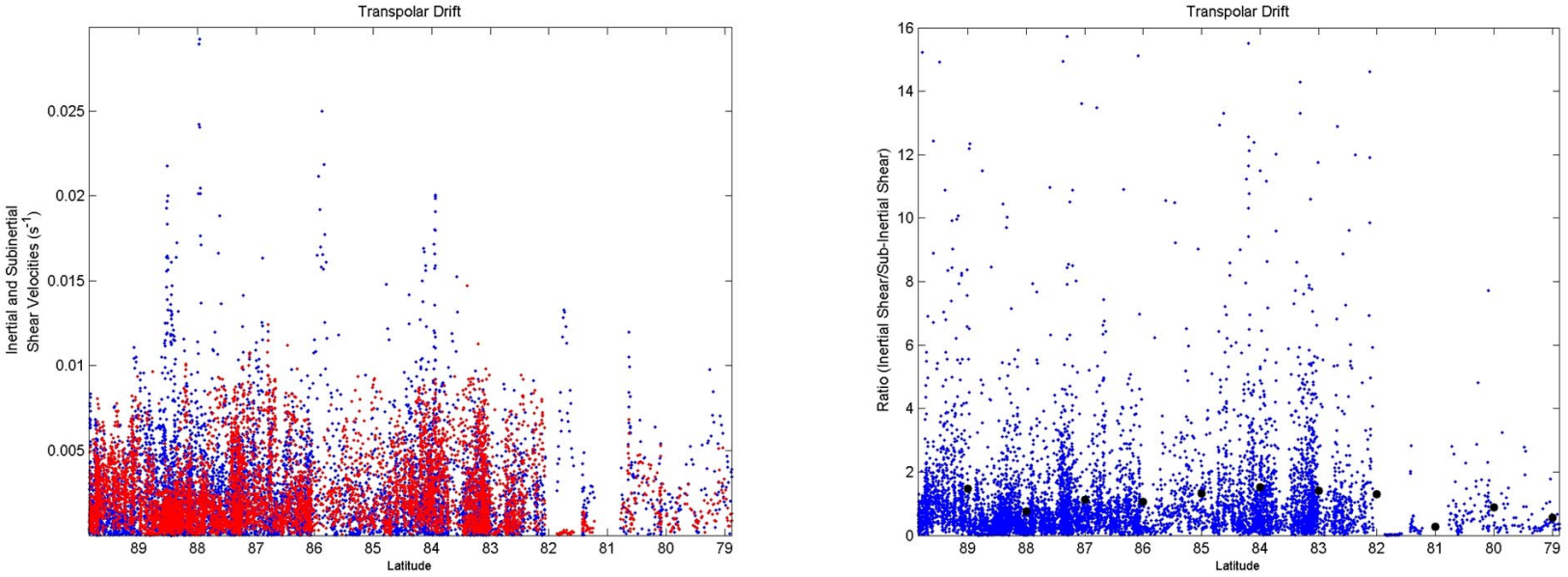

Figure 33. Inertial shear and subinertial shear measured at the base of the mixed layer with reference to latitude (left panel). Ratio between inertial shear and subinertial shear measured at the base of the mixed layer with reference to latitude (right panel). Black dots represent average latitude values.

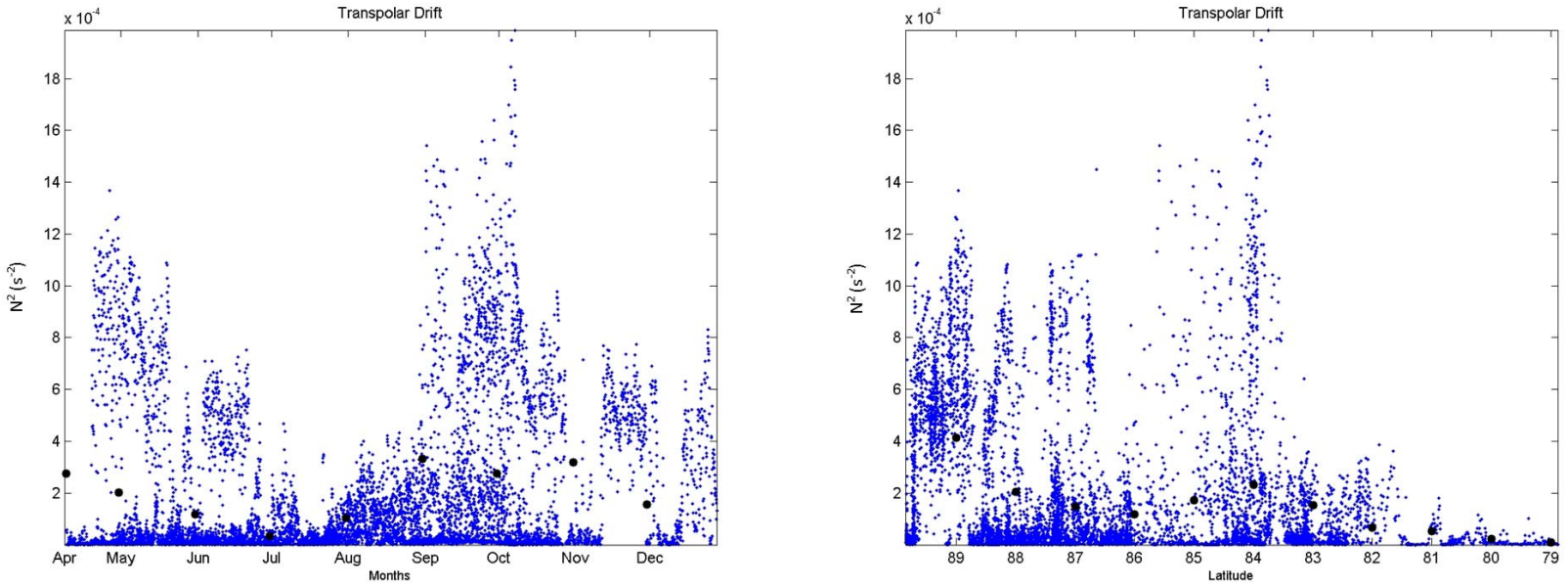

Figure 34. Time series of N^2 measured at the base of the mixed layer (left panel). N^2 measured at the base of the mixed layer with reference to latitude (right panel). Black dots for both figures represents average values.

We now determine how often the dynamic instability (quantified by Ri^{-1} total > 2) at the base of the mixed layer is supported by inertial motions. Like the Canadian Basin, it is hypothesized that occurrences of $Ri^{-1} > 2$ would occur greatest during summer, when the possibility of generating inertial motions is greatest due to freer sea ice. Monthly fractional occurrences of $Ri^{-1} > 2$ are shown in Figure 33 and Table 2. The largest occurrence of $Ri^{-1} > 2$ occurs during June, July, and August. Similar to the Canadian Basin, the majority of these months coincide with periods where increases in the ratio of inertial to subinertial shear velocities and decreases in stratification occur at the base of the mixed layer. During summer months (Jul-Sep), 26% of occurrences of 'Ri Total' would not occur unless supported by inertial shear velocities. These occurrences are much smaller during winter months (Oct-Dec) when 'Ri Total' needs the supplement of inertial shear 19% of the time. Again, similar to the Canadian Basin, the probability of observing 'Ri Total' in either season is about equal, ~54% in summer and ~57% in winter. The probability of 'Ri Inertial' occurring is greatest during summer with a probability of ~27% versus ~11% in winter. And the probability of 'Ri Sub-Inertial' occurring is greatest during winter with a probability of ~33% versus ~19% in summer. Again as it is in the Canadian Basin, in the Transpolar Drift it seems that inertial shear velocities occur and support shear enhanced turbulent mixing most during summer months where subinertial shear contributes the most during winter. Also, occurrences of 'Ri Total' and 'Ri Inert' for the Transpolar Drift are more frequent than those seen in the Canadian Basin due to the stronger winds towards the latter part of the year.

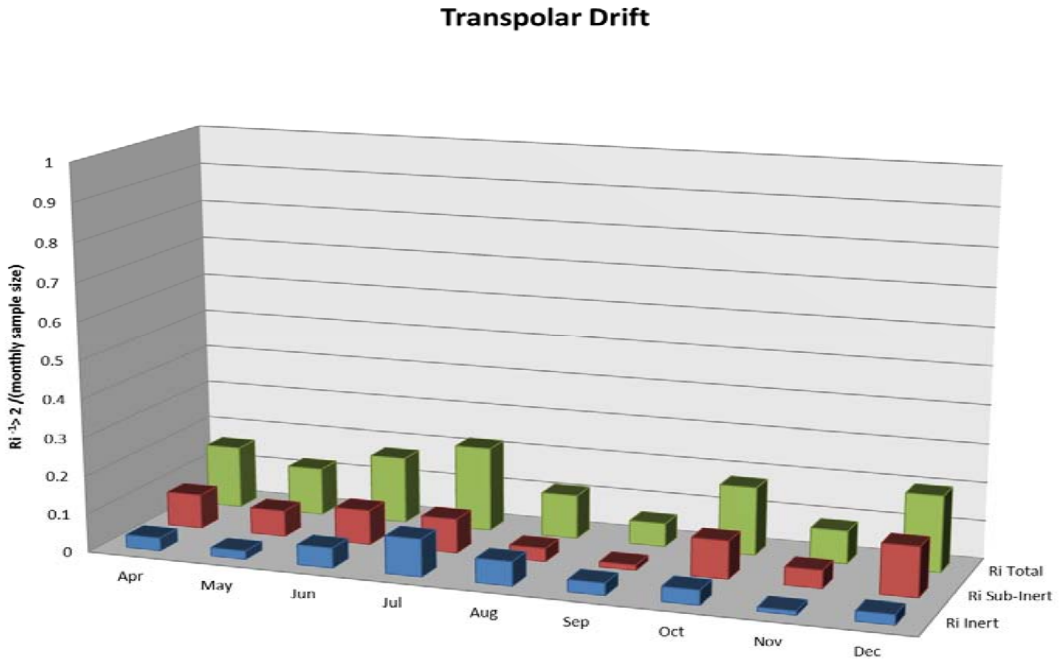

Figure 35. Monthly fractional occurrence of $Ri^{-1} > 2$ for the Transpolar Drift. ('Ri Total' calculated from subinertial and inertial velocities in green. 'Ri Sub-Inert' calculated from subinertial velocities in red. 'Ri Inert' calculated from inertial velocities in blue.)

	Apr	May	Jun	Jul	Aug	Sep	Oct	Nov	Dec
Ri Inert	0.0341	0.0224	0.0528	0.0986	0.0636	0.0322	0.0382	0.0111	0.0267
Ri Sub-Inert	0.09	0.0681	0.0907	0.0896	0.0349	0.0141	0.0996	0.0472	0.1306
Ri Total	0.163	0.1246	0.1741	0.2204	0.1147	0.0612	0.1778	0.0861	0.1988

Table 2. Values for monthly fractional occurrence of $Ri^{-1} > 2$ for the Transpolar Drift.

An analysis similar to the one conducted for the Canadian Basin is performed along the Transpolar Drift. Specifically, the inertial motion enhanced dynamic instability (quantified by 'Ri Inert' > 2) at the base of the mixed layer is compared to SSMI and AMSR-E derived ice concentration estimates to investigate whether the dynamic stability at the base of the mixed layer can be associated to sea ice concentration estimates.

Again, it is hypothesized that 'Ri Inert' > 2 will increase with decreasing satellite derived sea ice concentrations. Figure 36 shows that a slight trend exists when comparing 'Ri Inert' to SSMI sea ice concentration estimates, but it is too difficult to distinguish. Further, when comparing 'Ri Inert' to AMSR-E sea ice concentrations, a relationship does not exist. Also, the AMSR-E sea ice concentration estimates for this area is higher compared to the SSMI sea ice concentration estimates. From these observations, it can be determined that a relationship between 'Ri Inert' > 2 and satellite derived sea ice concentrations does not exist or is very difficult to discern. A relationship also does not exist or is hard to distinguish when comparing 'Ri Total' and 'Ri Sub-Inert' to satellite derived sea ice concentration estimates. Again, it should be noted that in section one, we found a tentative relationship between sea ice inertial motions and ice concentrations. Because mixed layer base stability is also dependent on stratification, it is unsurprising that the stability has no clear relationship to ice concentration.

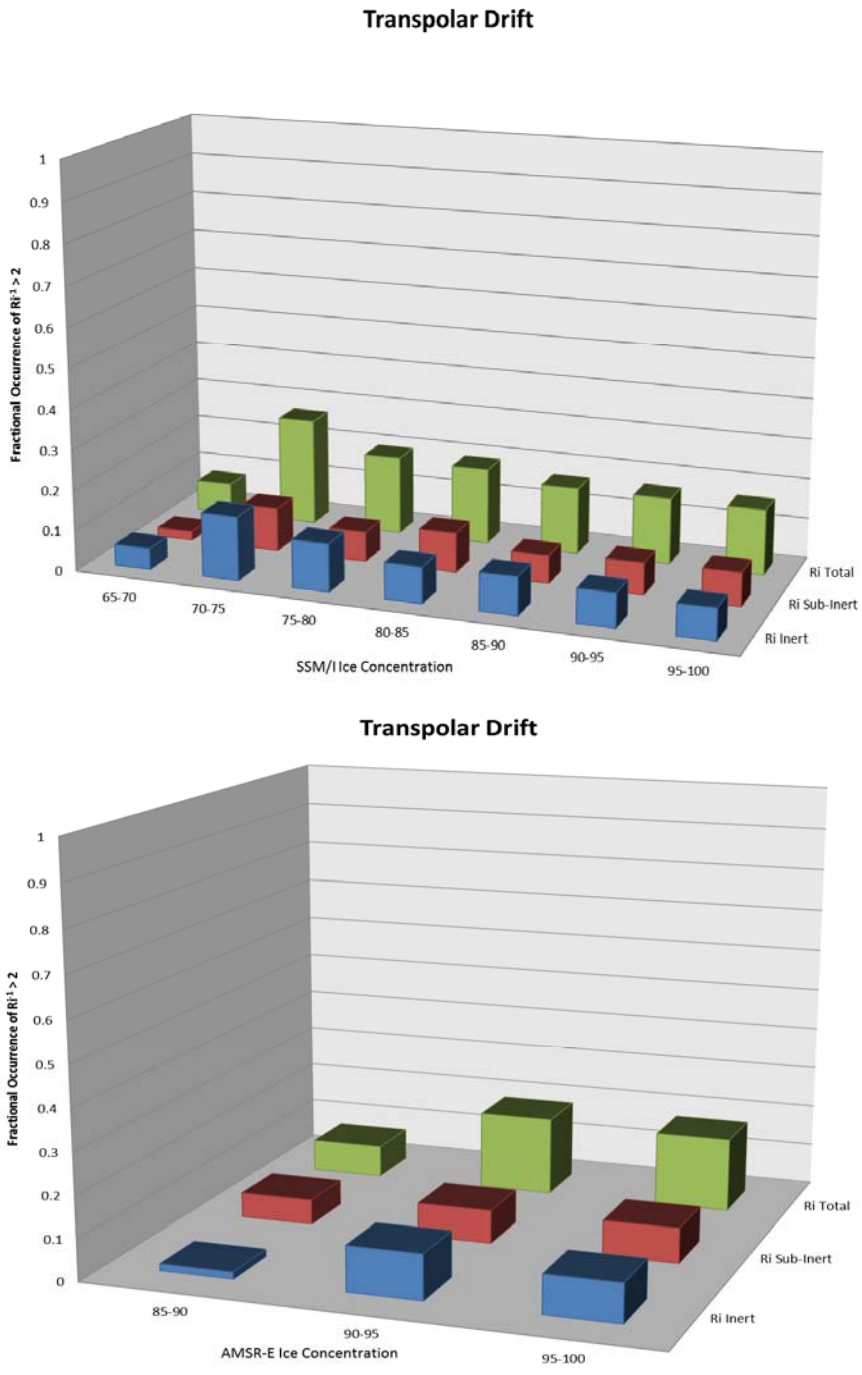

Figure 36. Top panel: $Ri^{-1} > 2$ compared to SSMI sea ice concetrations for the Transpolar Drift. Bottom panel: $Ri^{-1} > 2$ compared to AMSR-E sea ice concetrations for the Transpolar Drift. ('Ri Total' calculated from subinertial and inertial velocities in green. 'Ri Sub-Inert' calculated from subinertial velocities in red. 'Ri Inert' calculated from inertial velocities in blue)

IV. CONCLUSIONS AND RECOMMENDATIONS

A. SUMMARY

In recent years, there have been major changes in the Arctic Ocean including dramatic declines in sea ice and sea ice thickness. Numerical models have been created to simulate the observed sea ice decline and to predict the future states and conditions of the Arctic, but they have limitations in resolved physical processes and are conservative in their predictions of ice extent decline. This is in part due to the lack of observations and physical understanding of the small scale processes and mechanisms that occur below the sea ice, which contribute to bottom ablation of sea ice. Bottom ablation of sea ice can occur due to the entrainment of warmer waters beneath the cooler fresher waters of the Arctic Ocean mixed layer. There have been previous studies (Shaw et al., 2009 and Perovich et al., 2002) showing sea ice being affected by oceanic forcing and causing bottom ablation. Entrainment of warmer waters up into the Arctic Ocean mixed layer occurs by turbulent mixing. It has been previously investigated that mixing of the Arctic Ocean mixed layer can be initiated by storm driven winds (Yang et al., 2004). One of the physical processes manifested from these storm driven winds is inertial motions. This thesis focused on inertial motions and its role and influences on the Arctic Ocean mixed layer and sea ice decline.

In this study AOFB water velocity profiles, ITP CTD profiles, ECMWF winds, and SSMI and AMSR-E sea ice concentration estimates were used to analyze the relationships between wind forcing, state of the sea ice cover, and oceanic inertial oscillations in order to parameterize these characteristics. We also examine the effects of inertial motions on the dynamic stability at the base of the Arctic Ocean mixed layer. These analyses are done for both the Canadian Basin and the Transpolar Drift.

This thesis compares subinertial and inertial components of sea ice speeds to ECMWF modeled winds to determine if there is a linear relationship between the two, and whether inertial sea ice speeds can be parameterized using ECMWF modeled winds. Analysis shows that for the Canadian Basin and the Transpolar Drift simple linear

regression models cannot explain the relationship between inertial sea ice speeds and ECMWF modeled winds, although they do indicate that the magnitudes of the inertial sea ice speeds during summer months are greater when compared to winter months. Also, in one summer case study in the Canadian Basin, using data from AOFB 17, it was determined that inertial sea ice speeds were not related to the modeled inertial winds, but for the winter case study they were. This is an interesting observation and is recommended for further studies.

We then compared inertial sea ice speeds to SSMI and AMSR-E satellite derived sea ice concentrations. From the analysis we find that inertial sea ice speeds and satellite derived sea ice concentrations do show an inverse relationship between sea ice concentrations and inertial sea ice speeds. Observing these tendencies, we conclude that parameterizing the conditions that permit significant inertial motions in terms of changing areal ice conditions is viable; however, there are additional variables that must be investigated.

In our examination of the effects of inertial motions on the dynamic stability at the base of the Arctic Ocean mixed layer, we find that inertial motions do contribute to the unstable conditions at the base of the mixed layer. This is observed in our two case studies (summer and winter scenarios). Also, occurrences of instability at the base of the mixed layer for both regions occur most during summer time. Observing this relationship, we try to relate the dynamic instability at the base of the mixed layer to SSMI and AMSR-E satellite derived ice concentrations. Our analysis shows that it is difficult to establish a relationship between instability at the base of the mixed layer and sea ice concentration estimates from SSMI and AMSR-E sensors. This is expected, as seen from earlier results, as other factors such as stratification must also be taken into account. Sea ice concentration alone cannot explain the instabilities at the base of the Arctic Ocean mixed layer. From this analysis it was also observed that AMSR-E sea ice concentration estimates are higher when compared to SSMI sea ice concentration estimates for both regions.

B. FURTHER STUDIES

Several questions arose during this study. During our analysis of inertial sea ice speeds and satellite derived sea ice concentrations, AOFB 13 (located in the western Beaufort Sea in the marginal ice zone) depicted high inertial sea ice speeds during periods of high satellite derived sea ice concentrations, an observation that contradicts our hypothesis that inertial sea ice speeds should be dampened during this period. Thus, the question remains: is there an aspect of the marginal ice zone that allows for high inertial sea ice speeds while satellite derived sea ice concentrations are high?

Analysis of our two case studies showed that during the winter case study, the inertial component of ECMWF modeled winds shows a spike in amplitude prior to the observed inertial sea ice motion. On the other hand, in the summer case study this relationship was missing. Thus, future AOFBs should be equipped with atmospheric sensors to better understand the role of the atmosphere and sea ice generated inertial motions. With this, it would also be beneficial to study the effects of resonant wind forcing on exciting inertial oscillations.

Lastly, the cause behind the increase in the ratio of inertial to subinertial shear velocities at the base of the mixed layer earlier in the summer season when the inertial shear velocities itself are higher from mid to late summer should also be analyzed, since this earlier period coincides with periods of inertial motion supported dynamic instability at the base of the mixed layer.

THIS PAGE INTENTIONALLY LEFT BLANK

LIST OF REFERENCES

Arbetter, T. E., Curry, J. A., Holland, M. M., and Maslanik, J. A., 1997: Response of sea ice models to perturbations in surface heat flux. *Ann. Glaciol.*, **25**, 193–197.

Bush, G. W., President of the United States, 2009: National Security Presidential Directive - 66.

Cavalieri, D., M. Thorsten, and J. Comiso, 2004, updated daily. *AMSR-E/Aqua Daily L3 12.5 km Brightness Temperature, Sea Ice Concentration, & Snow Depth Polar Grids V002*, [2007-2010]. Boulder, Colorado USA: National Snow and Ice Data Center. Digital media.

Comiso, J., 1990, updated quarterly. *DMSP SSM/I Daily and Monthly Polar Gridded Bootstrap Sea Ice Concentrations*, [2007-2010]. Edited by J. Maslanik and J. Stroeve. Boulder, Colorado USA: National Snow and Ice Data Center. Digital media.

Curry, J. A., Ebert, E. E., 1995: Sea Ice-Albedo Climate Feedback Mechanism. Journal of Climate, **8**, 240–247.

D'Asaro, E. A., 1985: The energy flux from the wind to near-inertial motions in the mixed layer. *J. Phys. Oceanogr.*, **15**, 943 – 959.

European Center for Medium-Range Weather Forecasts, cited 2011: European Center for Medium Forecasts Experimental Analysis Interim (ERA-Interim). [Available online at http://www.ecmwf.int]

IPCC, 2007: Climate Change 2007: The Physical Science Basis. Contribution of Working Group I to the Fourth Assessment Report of the Intergovernmental Panel on Climate Change [Solomon, S., D. Qin, M. Manning, Z. Chen, M. Marquis, K.B. Averyt, M. Tignor and H.L. Miller (eds.)]. Cambridge University Press, Cambridge, United Kingdom and New York, NY, USA, 996 pp.

IPCC, 2007: Summary for Policymakers. In: Climate Change 2007: The Physical Science Basis. Contribution of Working Group I to the Fourth Assessment Report of the Intergovernmental Panel on Climate Change [Solomon, S., D. Qin, M. Manning, Z. Chen, M. Marquis, K.B. Averyt, M.Tignor and H.L. Miller (eds.)]. Cambridge University Press, Cambridge, United Kingdom and New York, NY, USA.

Halpern, D., 1974: Observations of the Deepening of the Wind-Mixed Layer in the Northeast Pacific Ocean. *J. Phys. Oceanogr.*, **4**, 454–466.

Hunkins, K. 1967: Inertial oscillations of Fletcher's Ice Island (T-3). *J. Geophys. Res.*, **72**(4), 1165–1174.

Naval Postgraduate School, cited 2011: Autonomous Ocean Flux Buoy. [Available online at http://www.oc.nps.edu/~stanton/fluxbuoy/index.html.]

Perovich, D. K., Grenfell, T. C., Light, B., and Hobbs, P. V., 2002: Seasonal evolution of the albedo of multiyear Arctic sea ice. *J. Geophys. Res*., **107**(C10), 8044, doi:10.1029/2000JC000438.

Perovich, D. K., Grenfell, T. C., Richter-Menge, J. A., Light, B., Tucker III, W. B., and Eicken, H., 2003: Thin and thinner: Sea ice mass balance measurements during SHEBA. *J. Geophys. Res*., **108**(C3), 8050, doi:10.1029/2001JC001079.

Perovich, D. K., J. A. Richter-Menge, K. F. Jones, and B. Light, 2008: Sunlight, water, and ice: Extreme Arctic sea ice melt during the summer of 2007. *Geophys. Res. Lett.*, **35**, L11501, doi:10.1029/2008GL034007.

Pollard, R. T., 1970: On the generation by winds of inertial waves in the ocean. *Deep Sea Research*, **17**, 795–812.

Pollard, R. T. and R. C. Millard, 1970: Comparison between observed and simulated wind-generated inertial oscillations. *Deep Sea Research*, **17**, 813–821.

Pollard, R. T., 1980: Properties of Near-Surface Inertial Oscillations. *Journal of Physical Oceanography*, **10**(3), 385–398.

Rudels, B., L. G. Anderson, E. P. Jones, 1996: Formation and evolution of the surface mixed layer and halocline of the Arctic Ocean. *J. Geophys. Res.*, **101**(C4), 8807–8821.

Serreze, M. C., Barrett, A. P., Slater, A. G., Woodgate, R. A., Aagaard, K., Lammers, R. B., Steele, M., Moritz, R., Meredith, M., and Lee, C. M., 2006: The large-scale freshwater cycle of the Arctic. *Journal of physical Research*, **111**. C11010.

Shaw, W. J., Stanton, T. P., Mcphee, M. G., Morison, J. H., and Martinson, D.G., 2009: Role of the upper ocean in the energy budget of Arctic sea ice during SHEBA. *J. Geophys. Res.*, **114**, C06012, doi:10.1029/2008JC004991.

Stroeve, J., Holland, M. M., Meier, W., Scambos, T., and Serreze, M., 2007: Arctic sea ice decline: Faster than forecast. *Geophysical Research Letter*, **34**, L09501, doi:10.1029/2007GL029703.

Task Force Climate Change / Oceanographer of the Navy, 2009: Navy Arctic Roadmap.

Task Force Climate Change / Oceanographer of the Navy, 2009: Navy Climate Change Roadmap.

Toole, J. M., Timmermans, M. L., Perovich, D. K., Krishfield, R. A., Proshutinsky, A., and Richter-Menge, J. A., 2010. Influences of the ocean surface mixed layer and hermohaline stratification on Arctic Sea ice in the central Canada Basin. J. Geophys. Res., **115**, C10018, doi:10.1029/2009JC005660.

Veronis G. and Stommel H.,1956: The action of variable wind stress on a stratified ocean. *J. Mar. Res*., **15**, 43–75.

Webster F., 1968: Observations of Inertial-Period Motions in the Deep Sea. *Rev. Geophys.*, **6**(4), 473–490 .

Woods Hole Oceanographic Institute, cited 2011: Ice Tethered Profiler. [Available online at http://www.whoi.edu/page.do?pid=20756.]

Yang, J., Comiso, J., Walsh, D, Krishfield, R., and Honjo, S., 2004: Storm-driven mixing and potential impact on the Arctic Ocean. *J. Geophys. Res*., **109**, C04008, doi:10.1029/2001JC001248.

Zhang, X., Walsh, J. E., 2006: Toward a Seasonally Ice-Covered Arctic Ocean: Scenarios from the IPCC AR4 Model Simulation. *Journal of Climate*, **19**, 1730–1747.

THIS PAGE INTENTIONALLY LEFT BLANK

INITIAL DISTRIBUTION LIST

1. Defense Technical Information Center
   Ft. Belvoir, Virginia

2. Dudley Knox Library
   Naval Postgraduate School
   Monterey, California

3. Dr. Timothy Stanton
   Naval Postgraduate School
   Monterey, California

4. Dr. William Shaw
   Naval Postgraduate School
   Monterey, California

5. Lieutenant George Suh
   Fleet Survey Team
   Bay St. Louis, Mississippi